

Chapter 1. Introduction

1.1 Motivation

Semiconductor nanoparticles attracted great attentions because of the beneficial electronic, magnetic, optic, and thermal properties, which are distinguished from bulk metal and single atom due to their high surface area and quantum size effects.¹ Based on these beneficial properties, nanostructured transition metal particles have a widely range of applications, such as photocatalysts utilized in photocatalytic process. Titanium dioxide is one of the most useful photocatalysts due to its high chemical stability, suitable band gap energy, low price and nontoxicity².

Heterogeneous photocatalysis has been a widely studied technology since 1970s and was an important water purification method in recent years. Photocatalysts generate a electron and hole pair to decompose the organic pollutants or reduce the heavy metal ions in water by illumination. Two broad categories of operating modes for photoreactors are slurry reactor utilizing suspended semiconductor metal oxide powders and immobilized reactor using photocatalysts immobilized on a substrate³.

Slurry reactor systems have the advantages of large specific surface area and the absence of mass transfer limitation due to the suspended nanometer-scale particles. The main drawbacks of slurry reactors can be attributed to the filtration requirements to retrieve the catalysts from the effluent stream and the limited penetration depth of the light into the slurry which may enhance the operating costs and lose the light efficiency⁴.

These barriers can be overcome by using immobilized reactors with nanoparticles immobilized onto the surfaces of solid supports. These carrier materials should be transparent to UV light, favor strong chemical-physical bonding with photocatalysts without reducing the photoactivity, facilitate to be separated from the liquid phase, and be chemical inert⁴. However, the main limitation of immobilized reactors is the limited mass transfer

due to the lower external mass transfer area and relatively low surface area. Catalysts immobilized on a porous support was developed to avoid these problems and enhance the photocatalytic activity due to the larger surface area applied from the porous structure. Therefore, the photocatalysts on the external surface will adsorb most of the incident light and hinder the illumination of photocatalysts inside the pores⁵. The surface of the catalyst may be attrited by the shear force resulting from the flow of the fluid and the immobilized nanoparticles may easily desorb from the surfaces of solid supports. These situations can lead to the filtration requirements due to the separated catalyst particles in the turbidity downstream and lose the original purpose.

In order to avoid the above drawbacks and maintain the advantage of large surface area, a great deal of research has been carried out to fabricate photocatalysts with porous structures to improve the photocatalytic properties in recent years. In addition, the photocatalysts with three-dimensional ordered porous architectures has been also developed due to the interconnected channels which can apply efficient transport paths for pollutant molecules to photocatalytic active sites on the pore walls⁶.

A number of methods have been developed to fabricate the ordered porous materials. Colloidal templating is one of the controllable and widely applicable methods to fabricate such structural materials. The basic fabrication is to use colloidal crystal as a template, infiltrate the interstitial spaces between the spheres of the template with another material and then selectively remove the template by chemical etching or calcination. Typically, latex/polystyrene (organic) and silica (inorganic) microspheres are the major types of particles that are usually used for the colloidal crystal assembly as they are highly monodisperse and relatively cheap. When the synthesis reaction takes place inside the interparticle voids of the template, the conditions in which the precursor is infiltrated and the template is removed and the chemical composition of the particles in the templating array are important factors that can also affect the wall microstructure and thickness of imprinted

porous oxides. However, the microstructures of which can affect the physical and chemical properties of porous oxides are hardly controlled.

The surface sol-gel process (SSP) was originally developed (Kunitake et al., 1997) and proved to be a superior technique for the preparation of ultrathin films of metal oxide-based gels with well molecular-scale control by means of stepwise adsorption of metal alkoxides and the simplicity of this process is a great advantage in commercial production of nanosized oxide films.

In order to fabricate the photocatalysts with high surface area, ascendancy in applications, low cost and well-controlled microstructures, we attempt to coat TiO_2 ultra-thin film onto porous and transparent SiO_2 matrix as bone-skin-like structure, which has not yet been developed, via template sol-gel and surface sol-gel methods.



1.2 Objective

The aim of this study was to fabricate highly porous SiO₂-TiO₂ photocatalysts as bone-skin-like structure by coating the TiO₂ ultra-thin films onto the highly porous silica with controllable film thickness and high photoactivity using the combination of template sol-gel and surface sol-gel methods. Monodisperse polystyrene microspheres in this study were prepared by emulsion polymerization method and used as templates to prepare ordered porous metal oxides.

To characterize the morphology and microstructures of polystyrene and porous materials, transmission electron microscopy (TEM), scanning electron microscope (SEM) and X-ray diffraction (XRD) were used. To measure the size distribution of polystyrene, the dynamic light scattering (DLS) was used. UV-visible spectroscopy and Brunauer-Emmett-Teller (BET) method were also used to measure the optical properties and specific surface areas of the porous photocatalysts as-prepared, respectively. Inductively coupled plasma mass spectrometry (ICP-MS) was used to measure the Si/Ti ratio of as-prepared samples.

And also to examine and compare the photocatalytic activities of the bone-skin-like SiO₂-TiO₂ with that of pure porous TiO₂ in terms of photodegradation of Rhodamine B.

The effect of interactions between photocatalysis efficiency and physicochemical properties of the photocatalysts, such as film thickness and the different crystalline size of TiO₂ were also investigated in this study.

Chapter 2 . Literature Review

2.1 Photocatalysis

2.1.1 Principle of photocatalysis

Photocatalysis has been a widely studied technology since the photocatalytic splitting of water on TiO₂ electrodes was discovered in 1972.⁷ Many investigations have been carried out with the aim of understanding the fundamental processes and enhancing photocatalytic efficiencies of the process. There is a widely range of environmental applications such as heavy metals recovery, water treatment, organic substance decomposition, disinfection, and hydrogenation presently based on the principle of photocatalysis.⁸

Semiconductors exhibit a void energy region that extends from the top of the valence band filled with electrons to the bottom of the vacant conduction band is called the band gap. If the semiconductor absorbs light with photon energy, $h\nu$, equal or greater than that of the band gap, a photon will excite an electron from the valence band to the conduction band, thereby generating an electron vacancy or a positive charge called a hole in the valence band (Figure 2-1).

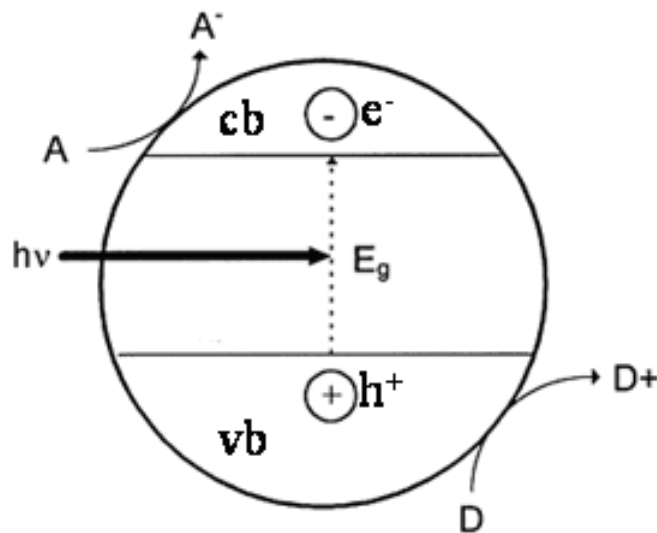


Figure 2-1 Reaction diagram of photocatalysis at a semiconductor by illumination.⁹

The electron-hole pair (e^-h^+ pair) can recombine on the surface or in the bulk of the particle in a few nanoseconds with producing thermal energy. The electron-hole pair also can migrate to the photocatalyst surface and then be trapped in surface states where it participates in redox reactions with the compounds adsorbed on the photocatalyst. In this redox reaction, these charges can react with electron donor (D) or acceptor (A) species adsorbed or close to the surface of the particle (Figure 2-2). The efficiency of a photocatalyst depends on the competition of different interface transfer processes involving electrons and holes and their deactivation by recombination.¹⁰

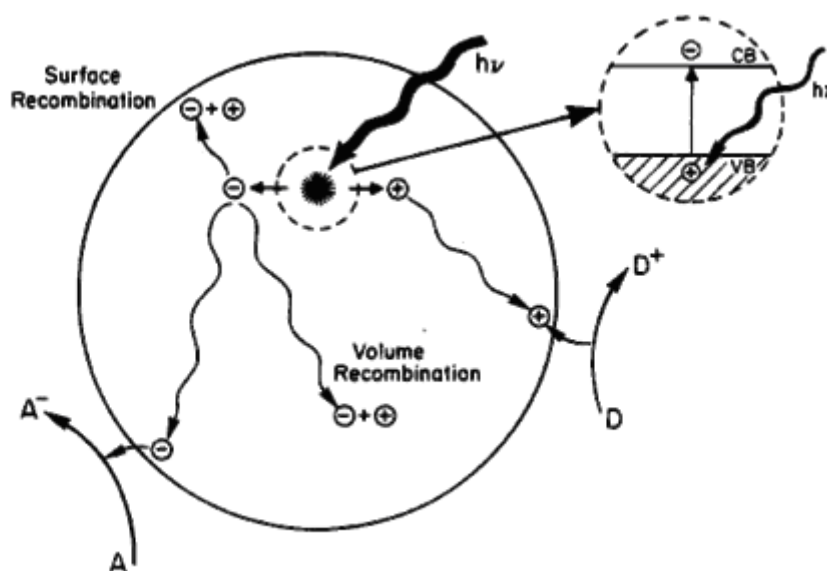


Figure 2-2 Schematic photoexcitation in a solid followed by deexcitation events.¹⁰

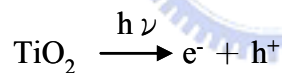
Thermodynamically, adsorbed compounds can be photoreduced by electrons in the conduction band if they have redox potentials more positive than the flatband potential of the conduction band, and can be oxidized by holes in the valence band if they have redox potentials more negative than the flatband potential of the valence band. The energy level at the bottom of the conduction band is actually the reduction potential of photoelectrons and the energy level at the top of the valence band determines the oxidizing ability of photoholes,

each value reflecting the ability of the system to promote reductions and oxidations.

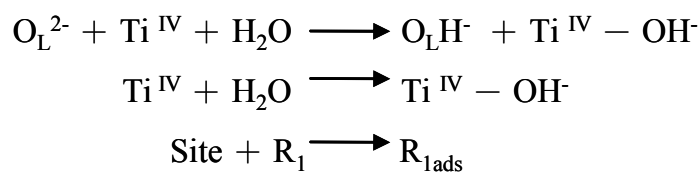
Generally, the hole oxidizes water to hydroxyl radicals (which subsequently initiate a chain of reactions leading to the oxidation of organics), or it can be combined with the electron from a donor species. Similarly, the electron can be donated to an electron acceptor such as an oxygen molecule (leading to formation of superoxide radical) or a metal ion (with a redox potential more positive than the band gap of the photocatalyst).

Turchi et al. described a photocatalytic reaction scheme for the degradation of organic water contaminants. The hydroxyl radical ($\text{OH} \cdot$) was proposed to be the primary oxidant in the photocatalytic system. Four possible mechanisms were suggested, all based on attack of the hydroxyl radical. The steps representing the proposed mechanisms can be expressed by the following set of simplified equations⁷:

Step I Excitation of the catalyst by photon energy greater than the band gap, generating electrons and holes

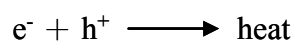


Step II Adsorption on the catalyst surface and lattice oxygen (O_L^{2-})

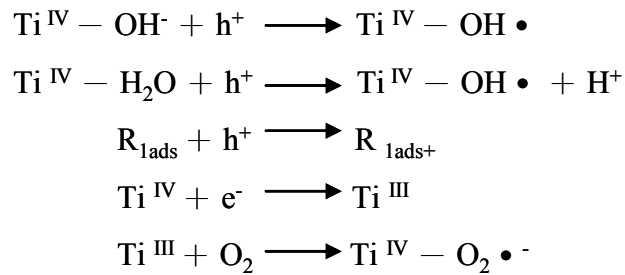


where R_1 represents an organic molecule, $\text{R}_{1\text{ads}}$ represents an adsorbed organic molecule

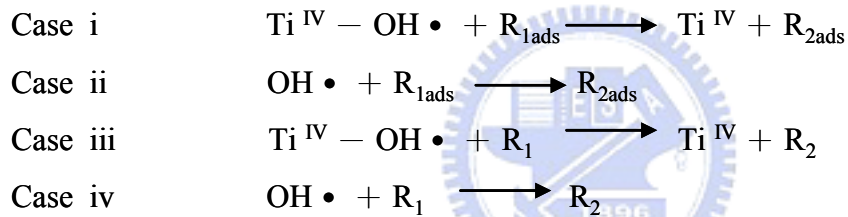
Step III Recombination of the $e^- - h^+$ pair, producing thermal energy



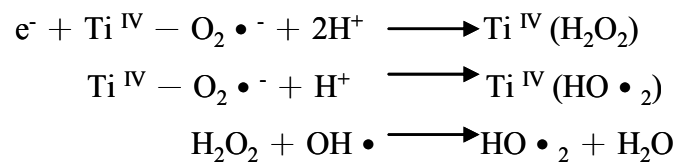
Step IV Trapping of the hole and electron



Attack of hydroxyl radical (adsorbed or free) under different conditions (adsorbed or free organic species)



Reactions of other radicals



2.1.2 Photocatalysts

Photocatalysts are usually provided with the properties of semiconductors. Unlike metals which have a continuous electronic states, semiconductors exhibit a void energy region in which no energy levels are available to promote the recombination of an electron and hole produced by photoactivation in the solid. If the semiconductor as the photocatalysts absorbs light with energy greater than that of the bandgap, a photon will excite an electron from the valence band to the conduction band, thereby generating a hole in the valence band. After these charges diffuse to the surface of the semiconductors, the oxidation or reduction of adsorbates can take place. Among a wide range of applications based on these principles, those related to environmental chemistry and pollution chemistry have been of interest recently.

The oxidizing and reducing abilities of the photocatalysts are related to the redox potentials of their valence band and conduction band. The band edge derived from the flat band potentials positions of several semiconductors in a contact solution of aqueous electrolyte at pH = 1 was shown in Figure 2-3. The band edge positions of titanium dioxide are -0.3 V and 2.9 V and its band gap energy are ranged from 3.02 eV to 3.2 eV.¹⁰

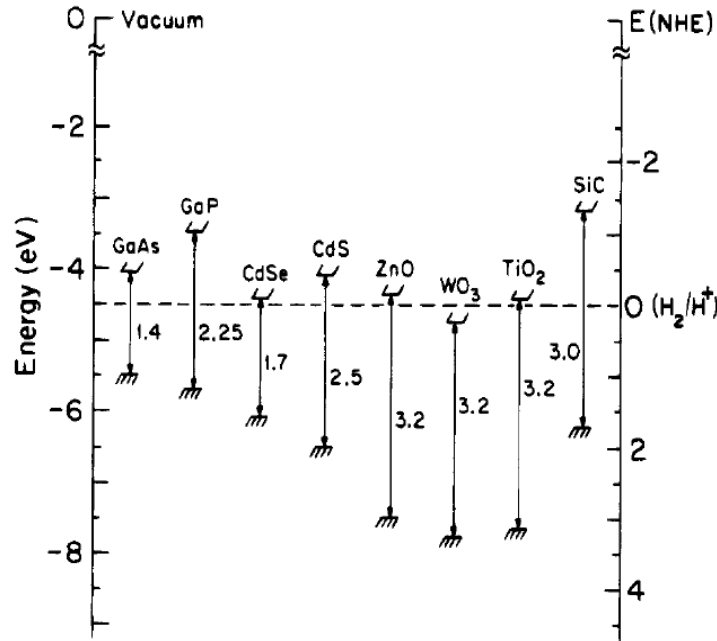


Figure 2-3 The band edge derived from the flat band potentials positions of several semiconductors in a contact solution of aqueous electrolyte at pH = 1.¹⁰

Titanium dioxide is one of the most useful photocatalysts presently. This is because of its exceptional optical and electronic properties, high chemical stability, low cost, nontoxicity, and suitable band gap energy that it can be excited to generate the electron-hole pair by UV rays with wavelength less than 410 nm. TiO₂ exists in three crystallographic forms, brookite, anatase and rutile. But only rutile and anatase are commonly used in photocatalysis, and the structures of rutile (3.02 eV, 411 nm) and anatase (3.23 eV, 384 nm) can be described in terms of chains of TiO₆ octahedral (Figure 2-4). Anatase is metastable phase and can transfer to rutile structure when heating at the temperature above 550 °C. In general, anatase are in general showing a higher photocatalytic activity than rutile, because of more oxygen vacancy sites as the active sites for photocatalytic processes of anatase structure and less bandgap energy about 3.23 eV.

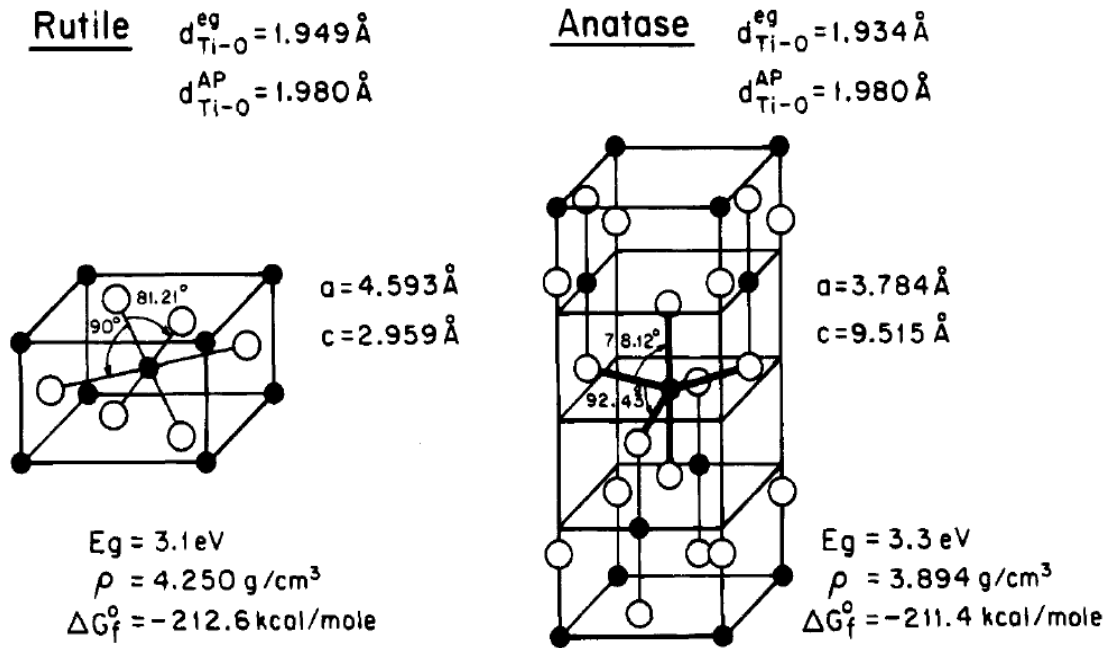


Figure 2-4 Structure of rutile and anatase TiO_2 .¹⁰

The most popular commercial form of TiO_2 is produced by the German company Degussa under the name P-25; this sample contains around 80% anatase and 20% rutile and possesses an excellent photocatalytic activity⁹. Recently, the band edge positions of the conduction band and valence band of Degussa P-25 have been calculated as -0.3 and $+2.9\text{V}$ ($\text{pH} = 0$), respectively (Figure 2-5).

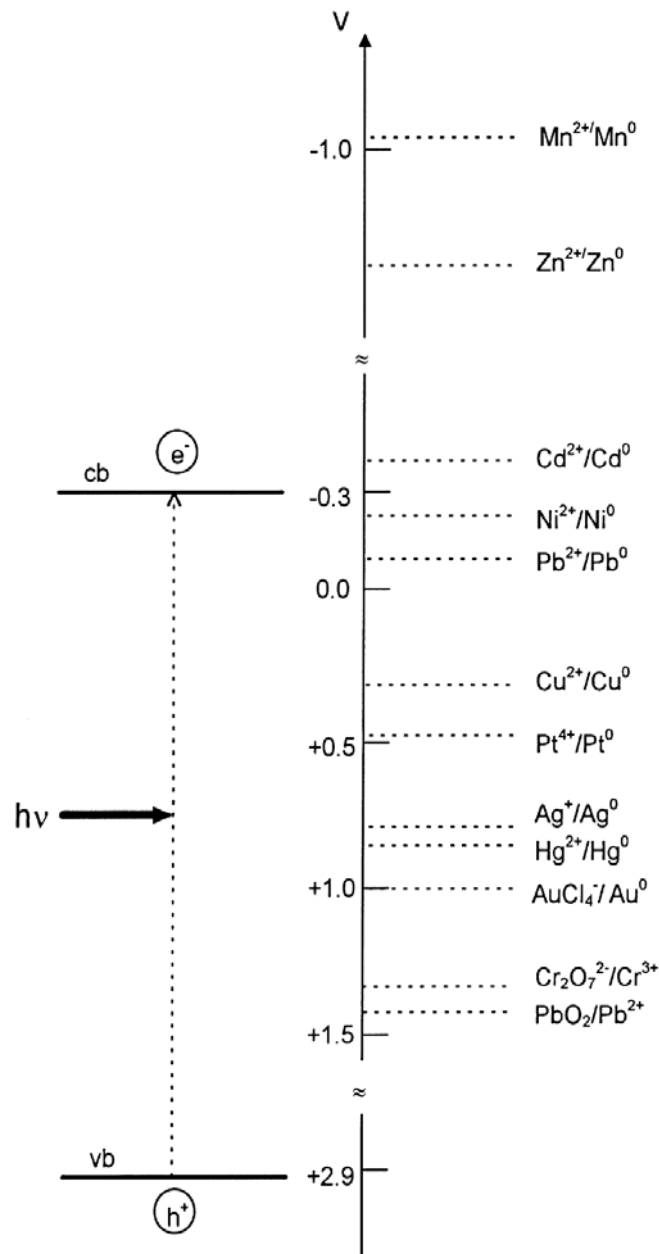


Figure 2-5 Positions of the redox potentials of various metallic couples related to the energy levels of the conduction and valence bands of TiO₂ Degussa P-25 at pH = 0.⁹

2.2 Colloidal crystal templating method

Ordered macroporous materials have attracted much attention in recent years due to their potential applications in various areas of separation processes, catalysis, photonic band gap materials, microelectronic and environmental engineering, and other emerging nanotechnologies.

A number of methods have been developed for the fabrication process, and colloidal templating is one of the controllable and widely applicable methods to fabricate such structural materials¹¹. Preparation of porous structures using colloidal crystal templating appears powerful, yet inexpensive and controllable, and could be adapted for large-scale production. The long-range ordering of the uniformly sized pores can eventually make these porous structures usable in high-technology applications.

A major advantage of the colloidal crystal template method is the ability to control the dimensions of the pores easily by varying the size of the particles in the templates. In addition, the versatility of this method is demonstrated through the use of both negatively and positively charged particles. Another advantage of colloidal crystal templating is its versatile application to a wide range of materials to make porous structures, including porous metals using a modified version of the method. And nearly all classes of inorganic and organic materials and metals have been templated into porous ordered structures¹².

But the main drawback of colloidal crystal templating is the additional procedure to remove the organic templates by calcinations or solvent extraction to form the solid porous skeleton and the pore size may decrease because of the contraction of porous structure during heat treatment.

The procedures involved in colloidal crystal templating method can be summarized into four steps¹³, as shown in Figure 2-6.

(a) Assembling of particles to form three-dimensional crystalline structure as template. The first step of the process is the assembly of the particles into a three-dimensional colloidal crystal matrix that will be used as a template for the replication of its long-ranged ordered structure to produce the porous material. The formation of three-dimensional colloidal crystal matrix from monodisperse particles can be induced by increasing their concentration in the vicinity of a flat surface by assembling methods such as sedimentation or filtration.

(b) Infusion of material into cavities of crystalline structure template. The interstices

(voids or vacant spaces between particles) of the template are infiltrated by the material of the porous structure in fluid or particle form.

(c) Solidification of material. The material in the interstices of the template will solidify to form the porous structure.

(d) Removal of template (particles) by calcination or solvent extraction. Finally, the particles are removed from the composite material either by solvent extraction (chemical dissolution) or calcinations (thermal decomposition) or other techniques, leaving behind a solid skeleton containing a three-dimensional ordered array of pores.

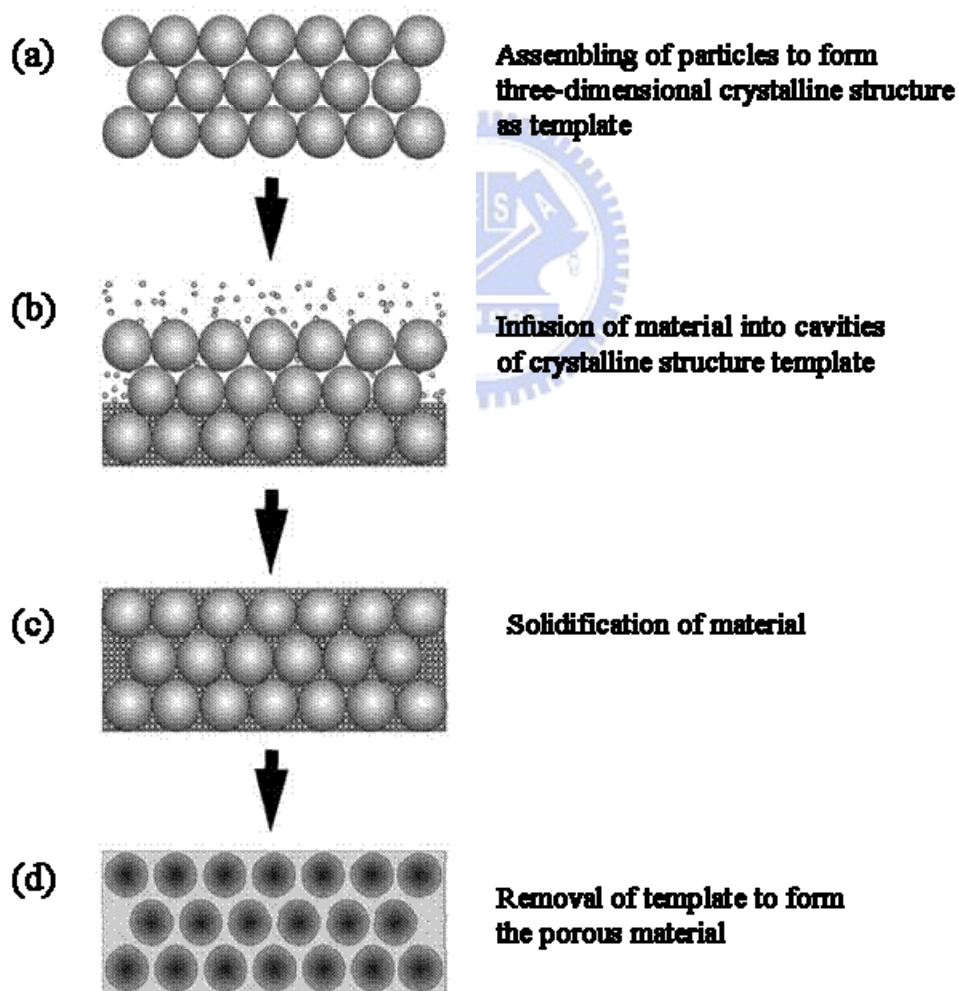


Figure 2-6 Schematic of the general procedure for replicating the structure of colloidal crystals into porous materials.¹³

Silica microspheres¹⁴ and latex such as polystyrene (PS) or poly(methyl methacrylate) (PMMA) latex spheres and emulsion droplets are the two major types of particles that are usually used for the colloidal crystal assembly because their highly monodisperse, relatively cheaply and easy to remove.

The solidified structure in the pores between the microspheres can be formed by a number of different strategies, such as surfactant/ UV/heat induced polymerization, sol-gel hydrolysis of a liquid precursor and electroless or electrochemical deposition precipitation. The sol-gel method is the most useful method because the imprinting method together with the advantages that sol– gel based processes offer, such as chemical homogeneity, high purity products and low processing temperature, have facilitated successful preparation of frameworks of periodic macroporous ceramics with different compositions.

When using colloidal crystal templating, a wide variety of porous materials, both organic and inorganic, can be produced. The different materials that can be used to make porous structure, the different types of particles used to construct the template and the methods of removing the particles after solidification of the porous material were summarized in Table 2-1.¹³

Table 2-1 Fabrication of porous materials by colloidal crystal templating.¹³

	Materials	Template	Template removal
Organic	PDMS	PS	PS not removed
	Polyurethane	PS	Dissolution in toluene
	Polyurethane, poly(acrylate-methacrylate) copolymer (PAMC)	Latex	Dissolution in toluene
	Divinylbenzene (DVB), PMMA, polyurethane, PS, PMA ethyleneglycol dimethacrylate (EDMA)	Silica	Etching with HIF
	Poly (2,5-dialkoxyphenylenevinylene)	Silica	Etching with HF
	Poly-allyl methacrylate (PAMA)	Silica	Etching with HF
Inorganic	Mixed metal oxides	PS	Calcination
	Titania	Silica	Etching with HF
	Silica	Latex	Dissolution in chloroform
	Composite metal oxides	PMMA	Sintering
	Aluminium oxide	PMMA	Calcination
	Tungsten nitride (infiltration by ALD)	Silica	Etching with HF
	Lithium niobate (LiNbO ₃)	PS	Calcination
	Titania (PMMA), zirconia (PMMA), silica (PMMA), Mercaptopropyl-functionalized silica (PS)	PMMA, PS	Calcination (PMMA) or solvent extraction (PS)
	Ni, Co, Fe, Ni-Co alloy	PMMA, PS	Calcination
	Silica, titania	PS latex	Calcination
	ZnO	PS	Calcination
	Titania, zirconia, PbTiO ₃ , Pb(ZrTi)O ₃	PS	Calcination or dissolution in toluene
	Mn ₃ Co ₇ , Ni-Co alloy	PMMA	Calcination
	Silica	PS latex	Calcination
	Titania, zirconia, silica, zeolites	Latex	Calcination or dissolution
	Titania	Latex	Calcination
	Graphite, glassy, carbon, diamond	Silica	Etching with HF
	CdSe	Silica	Etching with HF
	Titania, silica	Latex	Calcination
	NiO, metallic Ni	Latex	Calcination
	Ni, Cu, Ag, Au, Pt	Silica	Etching with HF
	Au	Latex	Calcination or dissolution
	CdSe, CdS	Latex, silica	Dissolution in toluene or HF

2.3 Principle of Emulsion Polymerization

Polymerization involves the linking together of small molecules of monomer to form a long-chain polymer molecule, also known as a macromolecule. Polymerizations in which the polymer chains grow exclusively by reaction of molecules of monomer with a reactive end-group on the growing chain are known as chain polymerizations. They usually require an initial reaction between the monomer and an initiator to start the growth of the chain.

Free-radical polymerization is the most widely practiced method of chain polymerization and is used almost exclusively for the preparation of polymers from olefinic monomers of the general structure $\text{CH}_2=\text{CR}^1\text{R}^2$, where R^1 and R^2 are two substituent groups which may be identical or different.

Emulsion polymerization is a free-radical-initiated chain polymerization in which a monomer or a mixture of monomer is polymerized in the presence of an aqueous solution of a surfactant to form a product, known as a latex. The latex is defined as a colloidal dispersion of polymer particles in an aqueous medium. The main ingredients for conducting these polymerizations include, in addition to the monomer and water, surfactants, initiators and chain transfer agents.

Water is a chief ingredient in both suspension and emulsion polymerization. As the continuous phase, it acts to maintain a low viscosity and provides for good heat transfer. In addition, it serves to isolate the polymerization loci. The water also acts as the medium of transfer of monomer from droplets to particles, the locus of initiator decomposition and oligomer formation, and the medium of dynamic exchange of surfactant between the phases.

The surfactant (also referred to as emulsifier) performs the dual function of providing sites for particle nucleation (i.e. monomer swollen micelles), as well as providing colloidal stability to the growing particles as a result of their adsorption at the particle-water interface. Even though anionic surfactants are commonly used in emulsion polymerization, other conventional surfactants are also used which include cationic surfactants (for making

cationically charged latex particles for special applications in paper coatings and asphalt additives), and non-ionic surfactants (for controlling latex particle morphology and for enhancing the post-polymerization colloidal stability against mechanical shear, freezing and added electrolytes). Reactive surfactants, which are surface active molecules with an active vinyl group, are also used in order to bind the surfactant chemically to the surface of the particles, with the advantage of reduced desorption during film formation and reduced water sensitivity of the latex films. Water-soluble polymers such as poly(vinyl alcohol), and hydroxyethyl cellulose can be used as the polymerization surfactants in order to impact stability against added electrolyte, mechanical shear, and freezing and thawing of the latex.

The most commonly used water-soluble initiator is the inorganic salt of persulfuric acid, such as potassium persulfate, which dissociates into two sulfate radical anions which can initiate the polymerization. Redox initiators, typically a mixture of an oxidizing agent and a reducing agent whose reactions generate radicals (such as persulfate-bisulfite), are typically useful for polymerization at low temperature. Oil-soluble initiators, such as azo compounds, are also used in emulsion polymerization in order to control particle morphology and grafting reactions within the particles, and to reduce the residual monomer at the end of the polymerization. A variety of chain transfer agents, such as mercaptans, are used primarily to control the molar mass of the polymer.

Emulsion polymerization can be divided into three stages: initiation, propagation and termination. In the first stage an initiator is used to produce free-radicals which react with the olefinic monomer to initiate the polymerization. There are two principal ways to form the free radicals: (1) homolytic scission (i.e. homolysis) of a single bond, and (2) single electron transfer to or from an ion or molecule (e.g. redox reactions). Homolysis is most simply achieved by the application of heat and there are many compounds which undergo thermolysis in the convenient temperature ranged from 50 to 100 °C. The most important initiators in his class are those possessing peroxide ($-O-O-$) or azo ($-N=N-$) groups.

Redox reactions often are used when it is necessary to perform polymerization at low temperatures. Each polymer chain propagates by rapid sequential addition of molecules of monomer to the terminal free-radical reactive site, which is known as the active centre for polymerization. There are two possible modes of propagation including head-to-tail linkages and head-to-head linkages (Figure 2-7). Termination of the growth of polymer chains results from reactions between actively growing polymer chains. Combination and disproportionation are the two most common termination reactions; both involve reaction between two growing polymer chains. Combination involves the coupling together of two growing chains to form a single polymer molecule and results in a head-to-head linkage at the point of coupling. In disproportionation, a hydrogen atom is abstracted from one growing chain by another, resulting in the formation of two polymer molecules, one with a saturated end-group and the other with an unsaturated end-group.

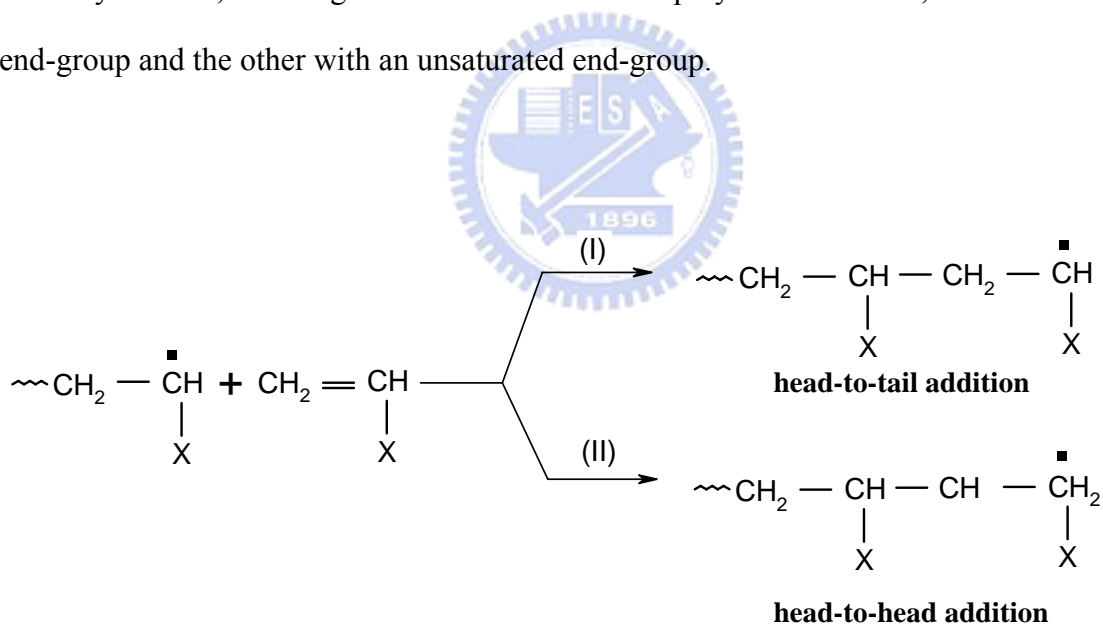


Figure 2-7 The two possible modes of propagation: (I) head-to-tail addition (II) head-to-head addition.

The process is usually considered as taking part in three stages which are illustrated schematically in Figure 2-8. The initiator generates a free radical and this is denoted by $\text{R} \cdot$.

Interval I: The initial polymerisation forms small latex particles.

Interval II: The particle nucleation has largely stopped. Initiator molecules diffuse through the water and become trapped in latexes (which consist of a mixture of the monomer and polymer chains) and thus bring about further polymerisation. At this stage the determination of polymer formation rate is governed by the availability of initiator molecules. There is a natural monomer/polymer ratio within the latexes and monomers are so freely available that their arrival is not rate determining. Successful mathematical theories of emulsion polymerisation assume that, at this stage, individual latexes contain either no initiator or actively growing polymer or, at the most, one of these.

Interval III: The monomer droplets have now all been consumed and the remaining initiator molecules gradually enter the existing latexes bringing about further polymerization and increasingly reduce the number of monomers contained in them.

If there is a large initial free-radical flux particles form rapidly and, at an early stage, become so numerous that they will capture all the free radicals in the aqueous phase before they can lead to the creation of new particles. The large free radical flux can be brought about both by the concentration of free radicals and also by working at a relatively high temperature. If very few new free particles are formed and the existing particles all grow at about the same rate an approximately monodispersive system will be produced.

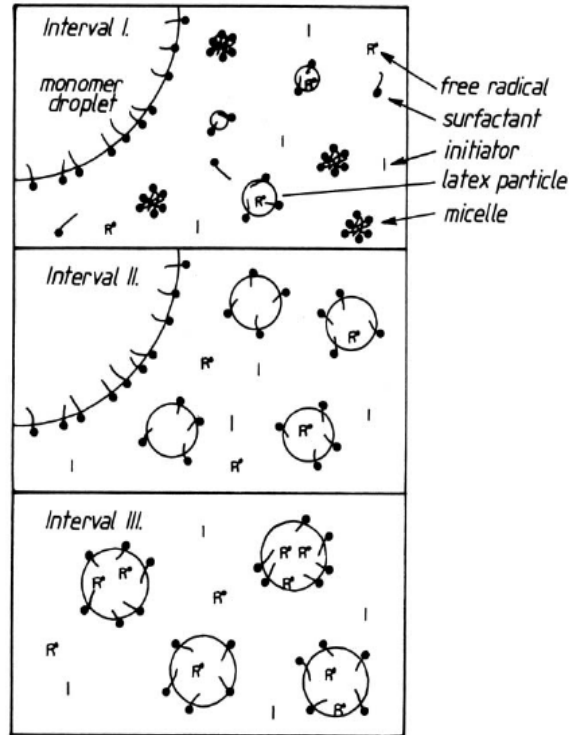


Figure 2-8 Schematic diagram illustrating the process of emulsion polymerisation.¹⁵

2.4 Sol-gel method

Sol-gel method is a kind of chemical reactions from colloid solution to solid gel phase and is mostly used in the fabrication of nanoparticles or thin films because of its facility, low cost and easy control of the nanoparticle size and morphology. Applying the sol-gel process, it is possible to fabricate ceramic or glass materials in a wide variety of forms: ultra-fine or spherical shaped powders, thin film coatings, ceramic fibers, microporous inorganic membranes, monolithic ceramics and glasses, or extremely porous aerogel materials¹⁶ (Figure 2-9).

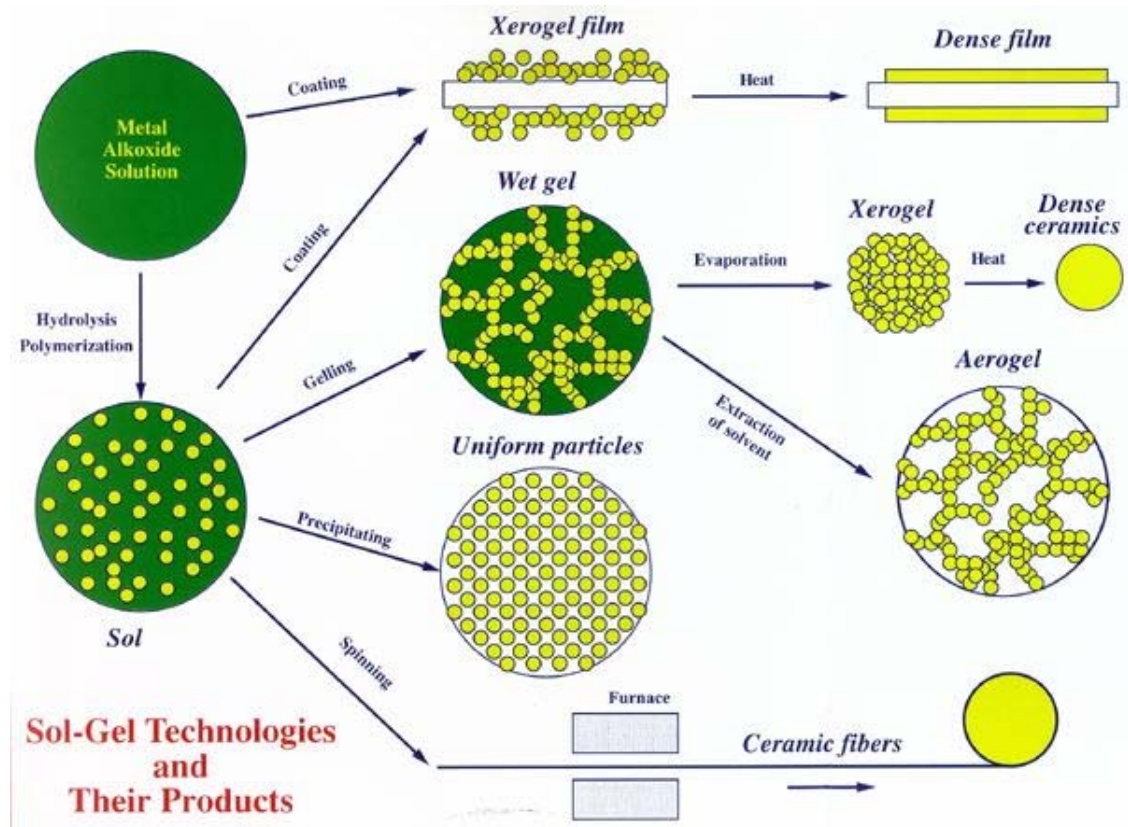
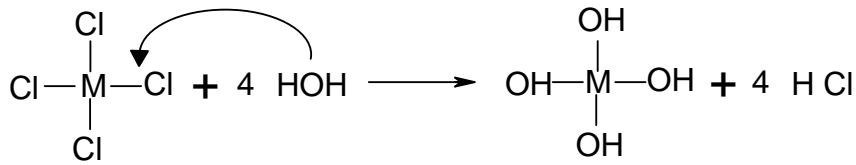


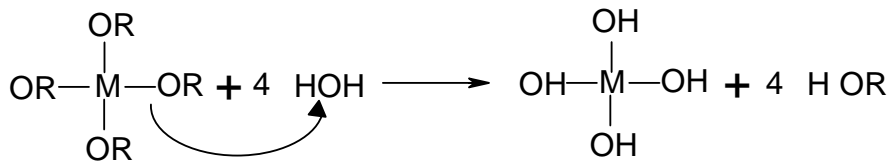
Figure 2-9 The sol-gel technologies and the various forms of products.

In generally, the precursor of sol-gel method is metal halide or metal alkoxide which reacts in the presence of water with alcohol as solvent. The mechanisms of sol-gel method including hydrolysis, condensation and gelation are shown in Figure 2-10. In hydrolysis, precursor will react with water to form the metal hydroxide first, and then the metal oxide dehydrate to form the oxo bond in condensation. A gel may be formed by network growth from by formation of an interconnected 3-D network by the simultaneous hydrolysis and polycondensation.

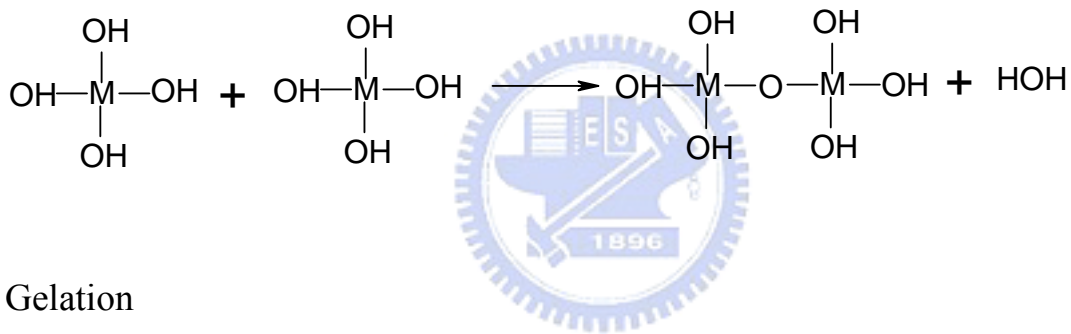
Hydrolysis



or



Condensation



Gelation

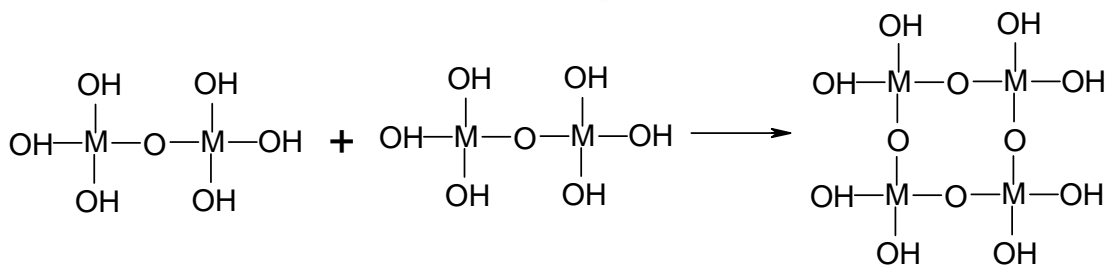


Figure 2-10 The reaction mechanism of sol-gel process.

Two catalytic reactions in hydrolytic sol-gel method, acid-catalyzed reaction and base-catalyzed reaction, use acid (HCl or HNO₃) and base (NH₄OH) as catalysts^{17,18}, respectively. These catalytic reactions can increase the rate of hydrolysis and decrease the condensation and gelation time. The mechanisms of acid-catalyzed reaction and base-catalyzed reaction belong to S_N1 and S_N2 reactions, respectively. Due to the different

mechanisms, the type of product in acid-catalyzed reaction is linear but the type of product in base-catalyzed reaction is non-shaped colloid. The pH value of precursor solution can effect not only the morphology of the products but also the reaction rate of hydrolysis and condensation. Except for acid or base, chelating agent can control the hydrolysis rate of precursor by forming the steric effect to decrease the hydrolysis rate and can also prevent the precipitation when preparing the coating solution. Besides, changing the relative ratio of chelating agent and precursor can control the reactive site of hydrolysis and the morphology of products. However, the most convenient and facile method to control the type of products is templating sol-gel method which combines template into sol solution and can form different pore structures of metal oxides or different types of nanoparticles through controlling the template types.

2.5 Surface Sol-gel method

Fabrication of metal oxide thin films with thickness control to nanometer precision is an important technology which leads to wide applications in future. Sol-gel method is one of the fabrications of metal oxide nanothin films and nanoparticles by using metal alkoxides or metal chlorides as precursors. There are three stages of the sol-gel reaction mechanism including hydrolysis, condensation and gelation. The main drawback of sol-gel method is difficult to fabricate ultra-thin films with molecular-scale. Several different techniques based on the layer-by-layer growth have been developed for this purpose since 1990s. For example, chemical vapor deposition technique has been applied to the preparation of one-atomic-layer metal oxides and thin-layer oxide catalysts.

The surface sol-gel process (SSP) was originally developed by Kunitake^{19,20} and co-workers in 1997. This novel technology enabled the preparation of the ultra-thin films of metal oxides with well molecular-scale control by means of stepwise adsorption of metal alkoxides. There are four steps included in surface sol-gel process: chemisorption of

alkoxide, rinsing, hydrolysis of the chemisorbed alkoxide, and drying (Figure 2-11). The substrate with surface hydroxyl groups, such as silicate, was first immersed into the precursor solution on the arid surrounding. The alkoxide groups of precursors can condense with the surface hydroxyl groups of the substrate and then chemisorbed on the surface of the substrate with monomolecular form. After rinsing with solvent to remove the physisorption on the surface of substrate, the substrate was immersed into the water and the surface chemisorbed precursors would hydrolysis to form the metal oxide thin film with molecular-scale. The film thickness of metal oxide ultra-thin film was determined by quartz crystal microbalance (QCM). For example, the film thickness of TiO_2 atomic thin film is about 8 Å. The regular film growth is achieved by repetition of saturated chemisorption of alkoxides and rinsing alone to form subsequent regeneration of a uniform hydroxyl surface.

The surface sol-gel process is a superior technique for the preparation of ultra-thin films of metal oxide-based gels with molecular precision and the simplicity of this process is a great advantage in commercial production of nanosized oxide films.

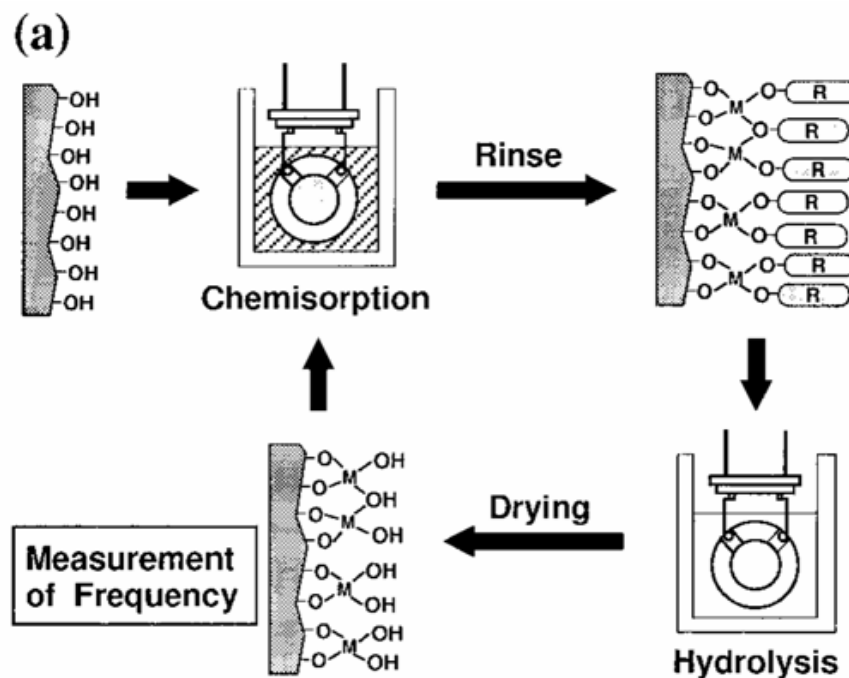


Figure 2-11 The four steps included in surface sol-gel process.¹⁹

Chapter 3. Materials and Methods

3.1 Chemicals

All chemicals were used as received without further treatment and the structures were shown in Table 3-1. Styrene (C_8H_8 , GC, >99 %), potassium persulfate ($K_2S_2O_8$, 99 %) and titanium isopropoxide ($Ti[OCH(CH_3)_2]_4$, 99.999 %) were purchased from Sigma-Aldrich Chemical Co., (St. Louis, USA). Sodium dodecyl sulfate ($C_{12}H_{25}NaO_4S$, >99%) was obtained from Merck Co. Inc., (Dortmund, Germany). Isopropanol ($CH_3CHOHCH_3$) was purchased from J. T. Baker Co., (New Jersey, USA). Hydrochloric acid (HCl , >35 %) was purchased from Crown Guaranteed Reagents. The precursor of SiO_2 , tetraethyl orthosilicate ($(C_2H_5O)_4Si$, TEOS, ≥ 99 %) was obtained from Fluka Co. Inc., (Tokyo, Japan). Polyoxyethylenesorbitan monolaurate (Tween 20) and Rhodamine B ($C_{28}H_{31}ClN_2O_3$, ~95 %) were also purchased from Sigma-Aldrich Chemical Co. Degussa P25 TiO_2 powders were provided from Degussa Corporation, Germany.

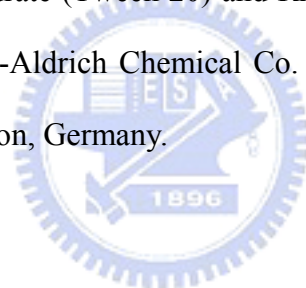
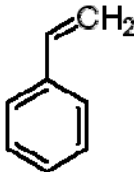
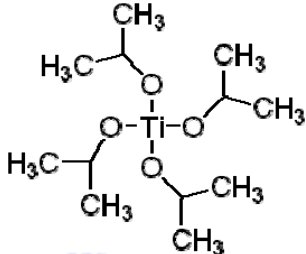
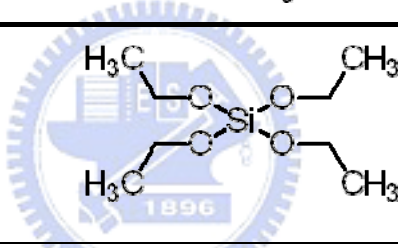
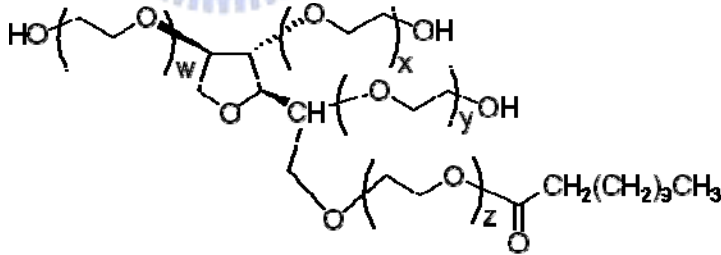
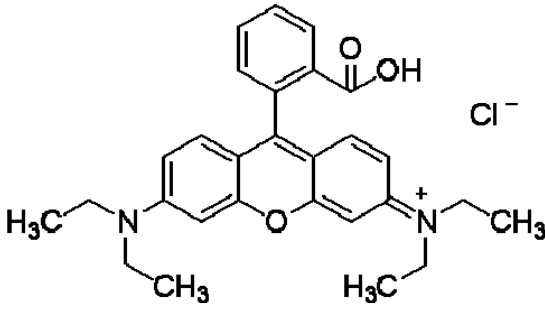


Table 3-1 The structures of chemicals used in this study.

Chemical	Structure
Styrene	
Sodium dodecyl sulfate	$\text{CH}_3(\text{CH}_2)_{10}\text{CH}_2\text{O}-\text{SO}_3\text{Na}$
Titanium isopropoxide	
Tetraethyl orthosilicate	
Tween 20	 <p>Sum of $w + x + y + z = 20$</p>
Rhodamine B	

3.2 Synthesis of polystyrene microspheres

Monodisperse polystyrene (PS) microspheres were prepared by oil-in-water emulsion polymerization in this study. The polymerization was carried out in a 50 ml round bottom flask equipped and a water-cooled reflux condenser was also included. Initially 39 ml of water were added to the flask, and then purged with nitrogen gas for 30 minutes with vigorously stirring at 350 rpm to maintain the anoxic condition. 1.4 mol l⁻¹ of styrene (as monomers) were added to the anoxic water and followed by adding sodium dodecyl sulfate (SDS) to control the mixture with various concentrations at 0.5 to 2 CMC. After stirring the mixture for 30 minutes, 2 mM of potassium persulfate (as initiator) were added to the reaction flask²⁰. In order to investigate the effects of the formation rate and the amounts of free radicals on the morphology and particle size of polystyrene, two different synthesis procedures, non-preheated and preheat procedures were used. In non-preheated treatment, 21.6 mg of K₂S₂O₈ was added into the flask containing of styrene and SDS under stirring at room temperature. On the contrary, the preheated procedure denoted that the initiator was added into the mixture at expect reaction temperature (70 ~ 90 °C).

The polymerization was carried out at various temperature ranged from 70 to 90 °C for 10 hours with a constant stirring at 350 rpm. Figure 3-1 showed the experimental device of polymerization. The flask was maintained at the required constant temperature (± 2 °C) by using a thermostatic silicon oil bath. After reacting for 10 hours, the polystyrene dispersions were formed. The mechanism of polymerization of polystyrene is showed in Figure 3-2.

In each case, the resulting latex was poured into a tube of dialysis membrane to separate the polystyrene from other reactants. The dialysis was sustained for one week against 2 L of deionized water.

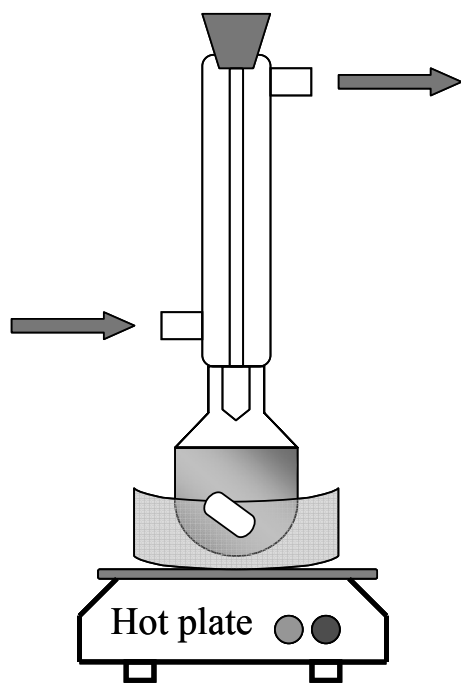


Figure 3-1 The experimental device of emulsion polymerization.

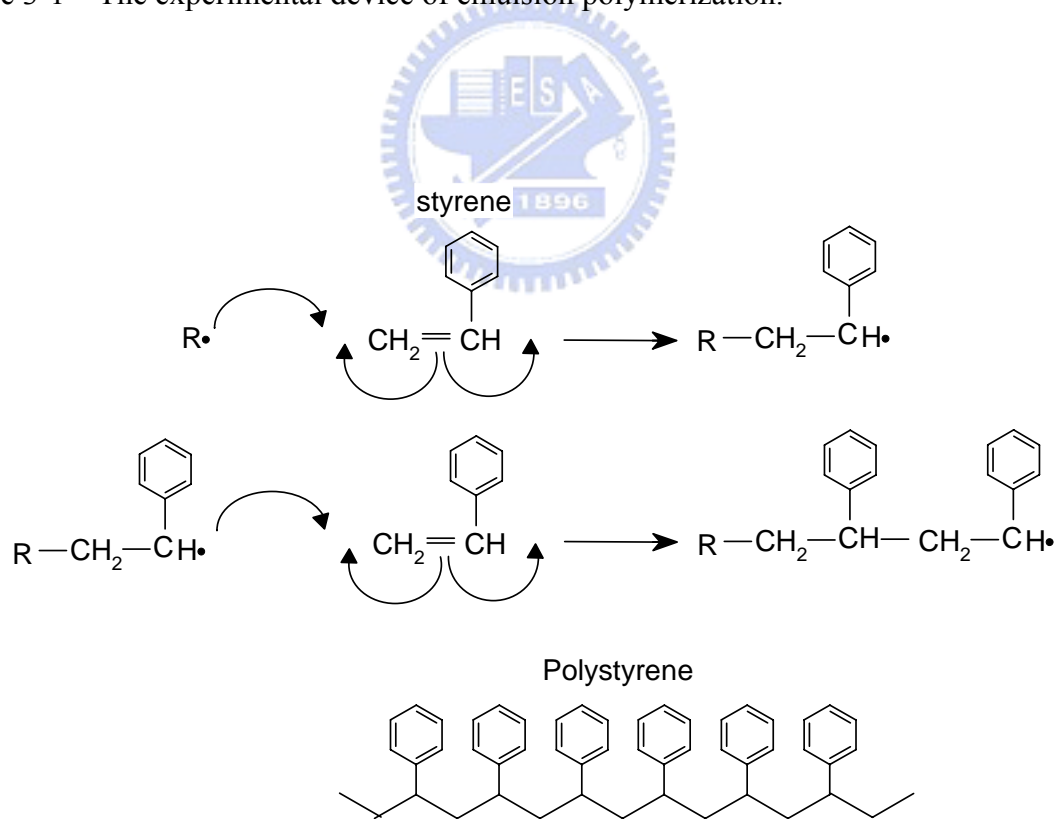


Figure 3-2 The mechanism of oil-in-water emulsion polymerization of polystyrene.

3.3 Fabrication of porous titania and silica

The ordered porous titania and silica were fabricated by templating sol-gel method combined with calcination in this study. Gravitational sedimentation of the particles combined with drying of the suspension was used to obtain the thick dry polystyrene latex arrangements as templates to prepare macroporous SiO₂ and TiO₂. 1 ml of dialysed polystyrene particles taken from the water-based dispersions were deposited on the cellulose acetate membranes with the diameter of 25 mm and pore size about 0.2 μm under atmospheric pressure and then dried at 50 °C. The oxides were obtained from solutions containing the inorganic precursors, which were confined inside the free space between the latex microspheres. The preparation of latex arrangements by deposition on filtration membranes was shown in Figure 3-3.

Titanium isopropoxide (Ti(OPr)ⁱ₄, TTIP) diluted in isopropanol was used as the sol solution of titania. In order to determine the variation of the properties of porous titania structures with different precursor concentrations, weight ratios of metal alkoxide/solvent of 0.2, 0.6 and 1.2 were used²¹. To ensure that spaces between spheres were filled by the solution before polymerization of the precursor, the precursor solution was acidified by addition of hydrochloric acid. Tetraethylorthosilicate (Si(OCH₂CH₃)₄, TEOS) diluted in ethanol absolute was used as the precursor of silica²⁰ and the precursor solution was also acidified by addition of hydrochloric acid with the volume ratio of TEOS/ethanol/HCl of 2:1:1.

The TiO₂ (or SiO₂) sol solution was introduced into the cavities of the latex arrays by using capillary forces. Figure 3-4 showed the addition of precursor solution to the template. 0.25 ml of the precursor of titania and 0.5 ml of the precursor of silica were added to the templates respectively. The template/metal oxide composite samples were dried at 30 °C and then calcined at 500 °C in air for 3 hours. The pure porous titania and silica were obtained after removal of templates by calcination.

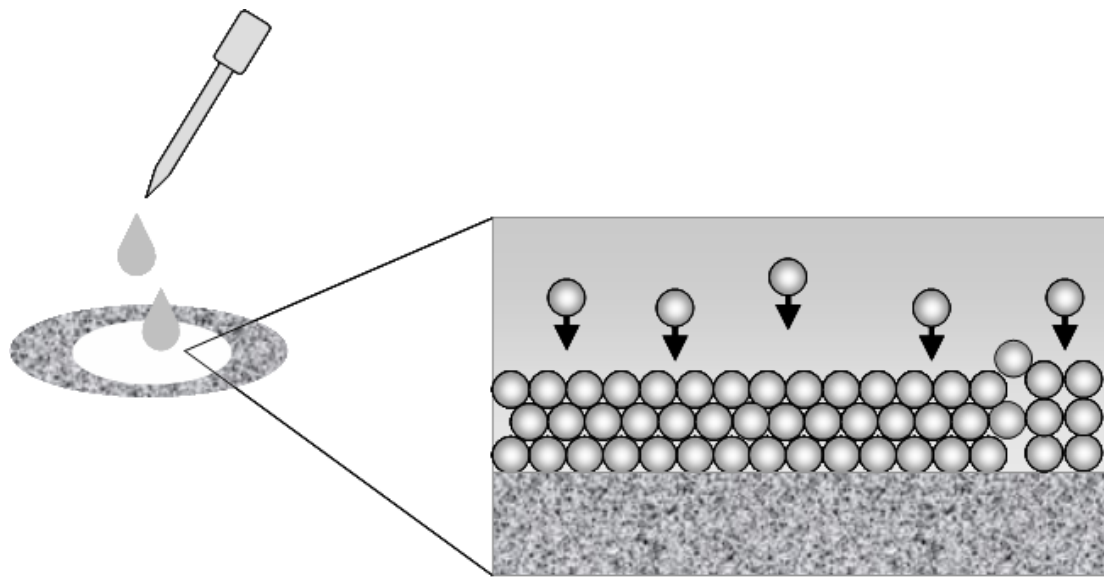


Figure 3-3 Preparation of latex arrangements by deposition on filtration membranes.

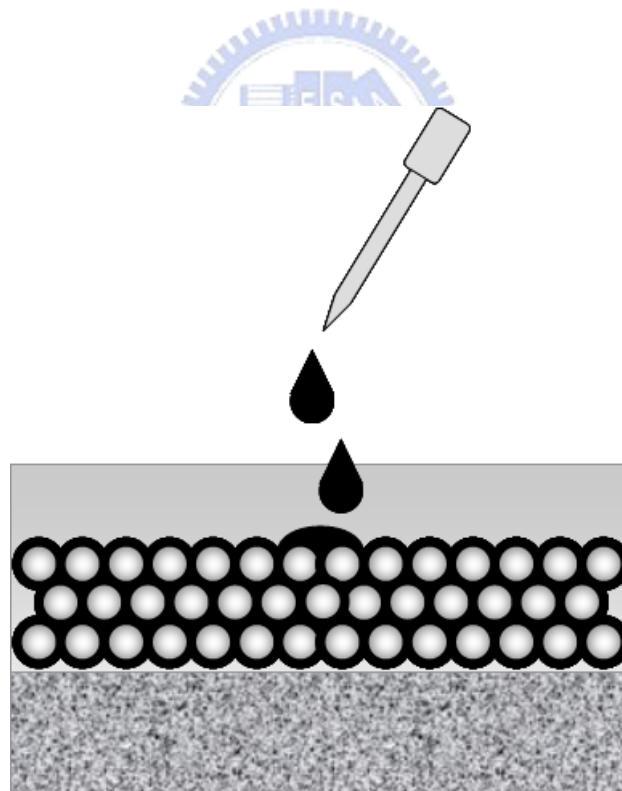


Figure 3-4 Schematic diagram illustrating the addition of precursor solution to the template.

3.4 Preparation of bone-skin-like photocatalysts

The bone-skin-like structures were obtained by coating the TiO₂ thin film (as skin) onto the surface of ordered porous SiO₂ (as bone) using surface sol-gel method in this study. The microfiltration assembly connected with a vacuum pump was used to obtain the surface sol-gel method.

In order to promote the affinity of TiO₂ sol solution to the surface of porous SiO₂ powder, Tween 20 was added to isopropanol to reach the concentration of 6 CMC. Titanium isopropoxide diluted in isopropanol with weight ratios of metal alkoxide/solvent of 0.2, 0.6 and 1.2 were used as the sol solution of titania. Commercial TiO₂ powder, Degussa P25, was dispersed in isopropanol to form TiO₂ slurry in order to discuss the effects of crystallinity and formation of TiO₂ coatings on the physicochemical properties of photocatalysts. Degussa P25 with various amount (36、72 and 135 mg) were added to 0.9 ml of isopropanol to reach the concentration of 0.2、0.6 and 1.2, respectively.

30 mg of porous SiO₂ powder was spread onto the filtration membrane and then 0.45 ml of the precursor solution of titania was added to contact with the SiO₂ powder under pumping. (Figure 3-5.) The glass support base was replaced by the filtration membrane (PVDF, 0.2 μm, 47 mm) to avoid the blocking of TiO₂ nanoparticles in the pores of glass support on purpose. If TiO₂ solution can pass through the pores of porous SiO₂ without intercurrent gelation, the TiO₂ ultra thin film will form successfully on the surface of porous SiO₂. In order to ensure the above situation, the procedure was operated under the pressure of 160 mmHg.

The SiO₂ powder/TiO₂ precursor composite samples were dried at 30 °C and then calcined at 500 °C in air for 3 hours.



Figure 3-5 The experimental device of the preparation of bone-skin-like photocatalysts.

3.5 Photodegradation of Rhodamine B

In order to compare the photocatalytic activities of pure TiO_2 porous structures and bone-skin-like photocatalysts, the photoactivities of as-prepared samples were detected by the degradation of Rhodamine B²² which is used in biology as a staining fluorescent dye at ambient temperature. The commercial photocatalysts, Degussa P-25, were also used to compare the photocatalytic activities with the porous photocatalysts we prepared. The initial concentration of Rhodamine B solution was 0.05 mM. The aqueous Rh B/photocatalysts dispersions were prepared by the addition of photocatalysts (15 mg) into a 15 mL aqueous solution containing Rh B dye.

Prior to the irradiation, the suspensions were sonicated for 30 min to reach adsorption/desorption equilibrium of the Rh B on the surface of TiO_2 . The mixtures were

purged by oxygen for 30 min in the dark to ensure the saturated dissolved oxygen of the solution and then irradiated by Ultraviolet lights with wavelength at 305 nm in a photoreactor (Figure 3-6.). During illumination, the samples were purged ceaselessly by O₂ to maintain the saturated dissolved oxygen and the adequate suspension of photocatalysts in the dye solution. The mixtures were sampled every 5 min and diluted with DI water. The decoloration of Rh B was measured the absorbance using UV-Visible Spectroscopy.



Figure 3-6 The instrument of photoreactor.

3.6 Characterization

All the samples were characterized in terms of SEM · TEM · HRTEM · XRD · UV-Vis · BET · ICP-MS and EPR in this study. Polystyrene arrays and morphology were characterized by scanning electron microscopy (SEM). The samples were coated with a gold film before observed in a Hitachi, S-4700 , Type II electron microscopy working at 25 kV. The microstructures of porous materials were characterized by transmission electron microscopy (TEM) taken with a Hitachi, H-7500 electron microscopy operating at 120 kV. The structure and the crystallinity of the resultant porous materials were characterized using X-ray diffraction (XRD) (MAC Science, MXP18) with Cu K α radiation ($\lambda= 0.15406$ nm). The other operational parameters of XRD were listed in the appendix (Appendix A-1.). The crystalline size are calculated from the broaden of the deflection peaks based on the Scherrer's equation. UV-Vis spectra were measured on a UV-visible scanning spectrophotometer (HITACHI U-3010) with Al₂O₃ as an internal standard. The other operational parameters of UV-vis were listed in the appendix (Appendix A-2.). Reflectance (%R) results obtained from HITACHI U-3010 are translated to absorbance by the Kubelka-Munk formula. The specific surface area was determined according to the Brunauer-Emment-Teller (BET) method. The pore size distributions were obtained from the analysis of the adsorption branch of the isotherm by the Barrett-Joyner-Halenda (BJH) method. The total pore volume was obtained from the volume of nitrogen adsorbed at a relative pressure of 0.95. In order to estimate the real mass of titania of bone-skin-like structure, inductively coupled plasma mass spectrometry (ICP-MS) (Perkin Elmer · SCIEX ELAN 5000) was used to measure the Si/Ti ratio of as-prepared samples.

Chapter 4 . Results and Discussion

4.1 Preparation of Polystyrene Microspheres

4.1.1 Effect of heating procedure and surfactant concentration

Emulsion polymerization involves formation of styrene droplets via oil-in-water emulsions and polymerization of the styrene by radicals generated from thermolysis of initiators. The shapes of micelles and formation rate of the free radicals dominate the morphology and particle size of polystyrene in the emulsion polymerization process and they are greatly dependent on concentration of surfactants and heating history during preparation. In order to understand the optimal conditions for monodispersed and uniform shaped and sized polystyrene microspheres, the emulsion polymerization was carried out in the presence of different concentrations of SDS and under different heating procedures.

Figure 4-1 shows the SEM images of polystyrene microspheres prepared under various conditions. The results of two different heating procedures, non-preheated and preheated treatment, at reaction temperature about 70 °C with the same surfactant concentration of 1 CMC were shown in Figure 4-1 (A) and (B). This result indicates that the polystyrene particles prepared in the preheated procedure demonstrate the better dispersion than that in the non-preheated procedure at the same reaction temperature and surfactant concentration.

Figure 4-1 (B) ~ (D) showed the SEM images of polystyrene synthesized at 70 °C with preheated treatment and various surfactant concentrations of 0.5 CMC 、 1 CMC and 2 CMC. The spherical particles of polystyrene prepared with surfactant concentration of 0.5 CMC were monodisperse with a diameter of about 270 nm. Non-uniform particle size and non-spherical morphology of polystyrene microspheres could be observed at high surfactant concentrations. This phenomenon was discussed below. Casey et al. described that micellar and homogenous nucleation were both the main mechanisms of particle formation when the particles were formed with surfactant concentrations above the cmc. In these two

mechanisms, the surfactant concentration is directly related to the latex particle size and the colloidal stability by adsorbing surfactant molecules on the surface of primary particles. High surfactant concentration may cause non-uniform surfactant adsorption of primary particles and a large number of surfactant molecules distributed on the surface of the droplets may hinder the diffusion of free radicals into the monomer droplets to initiate the polymerization. This situation may cause different polymerization rates and result in non-uniform particle size and non-spherical morphology of polystyrene latex particles.



4.1.2 Effect of reaction temperature

The free radicals which initiated the polymerization were formed by thermolytic scission of a single bond of initiators. The reaction temperature related to the formation rate and the amounts of free radicals could also affect the morphology and particle size of polystyrene synthesized with emulsion polymerization.

Three reaction temperatures, 70 °C, 80 °C and 90 °C, were chosen to estimate the effect of the reaction temperature on the morphology of resulting polystyrene spheres. Figure 4-1 (E) and (F) show the SEM images of polystyrene synthesized with preheated treatment at 80 and 90 °C with surfactant concentration of 1 CMC, respectively. The results of reaction temperature at 70 and 90 °C do not show the optimal morphology, uniform size distribution and ordered array. The optimal condition observed in Figure 4-1 (H) is heating at 80 °C in preheated procedure when 1 CMC of SDS was used as stabilizer. The uniform particle size of polystyrene is almost 190 nm and the three-dimensionally ordered array of polystyrene can be observed in this condition. It might be the result of the balance of relatively high temperature and suitable surfactant concentration.

If there is numerous initial free-radical flux particles formed rapidly at early gradation, these particles will trap the free radicals in the aqueous phase before they can lead to the creation of new particles. The large free radical flux particles can form at a higher temperature in the system and all the existing particles can grow at the same rate. In this condition, an approximately monodispersive system will be produced and the resulting latex particles will form with uniform particle size and spherical morphology.¹⁵ In this study, polymerization carried out at relatively high reaction temperature with preheated procedure and suitable surfactant concentration can obtain this monodispersive system.

Owing to the result, the polystyrene synthesized at 80 °C in preheated procedure when 1 CMC of SDS was added is used as the template in the following experiments.

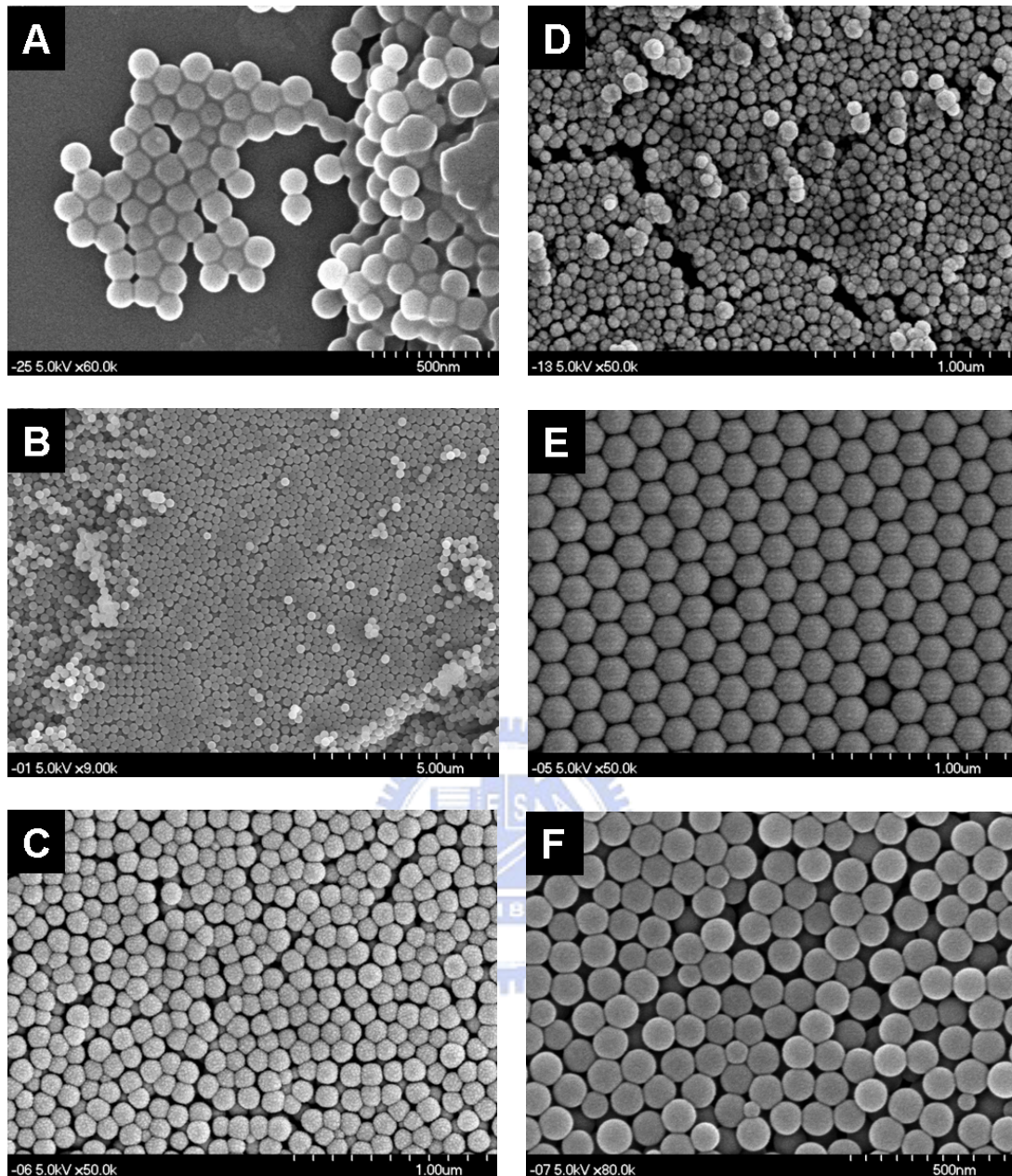


Figure 4-1 SEM images of polystyrene synthesized under various conditions : non-preheated treatment at 70 °C with surfactant concentration of 1 CMC (A) and preheated treatment at 70 °C with various surfactant concentrations (B) 0.5 CMC, (C) 1 CMC and (D) 2 CMC of SDS. Preheated treatment at 80 °C with surfactant concentration of 1 CMC (E) and preheated treatment at 90 °C with surfactant concentration of 1 CMC (F).

4.2 Morphology of Porous TiO₂ and bone-skin-like SiO₂/TiO₂

Porous metal oxides were prepared by infiltration of the void of polystyrene 3D colloidal crystals with sol solutions of metal oxides followed by removal of the polystyrene microspheres. To understand the effect of sol-gel kinetics on the microstructures of the porous metal oxides, the sol solution with different metal alkoxide/solvent weight ratios were used for sample preparation.

Figure 4-2 shows the TEM and SEM images of the porous TiO₂ prepared by the sol solutions with the TTIP/isopropanol weight ratios of 0.2, 0.6 and 1.2. The TEM and SEM images indicate that the TiO₂ consist of ordered hexagonal porous structures in three dimensions. Table 4-1 lists the wall thickness, pore sizes and shrinkages of the porous TiO₂ and porous SiO₂/TiO₂. The wall thickness of porous TiO₂ increased from 33 to 42 nm when the TTIP/isopropanol weight ratios increased from 0.2 to 1.2. This result indicates that the concentration of precursor in the sol solution dominates the wall thickness of the porous TiO₂. Moreover, the thicker wall obtained from more concentrated sol solution is probably due to high viscosity. Viscous sol solutions poorly penetrate the colloidal crystal templates so that expand the space between PS microspheres. The high viscosity of concentrated sol solutions has been demonstrated in many literatures. The pore sizes of the porous TiO₂ were ranged from 133 to 149 nm with increasing precursor concentrations. The pore sizes were smaller than the sizes of PS microspheres, indicating that calcination shrinks about 21 to 33 % of the templated pores. The disordered porous structure was obtained when the TTIP/isopropanol weight ratio was 1.2. It is presumably due to that fast gelation and high viscosity of the concentrated sol solution disorders the PS colloidal crystals during infiltration.

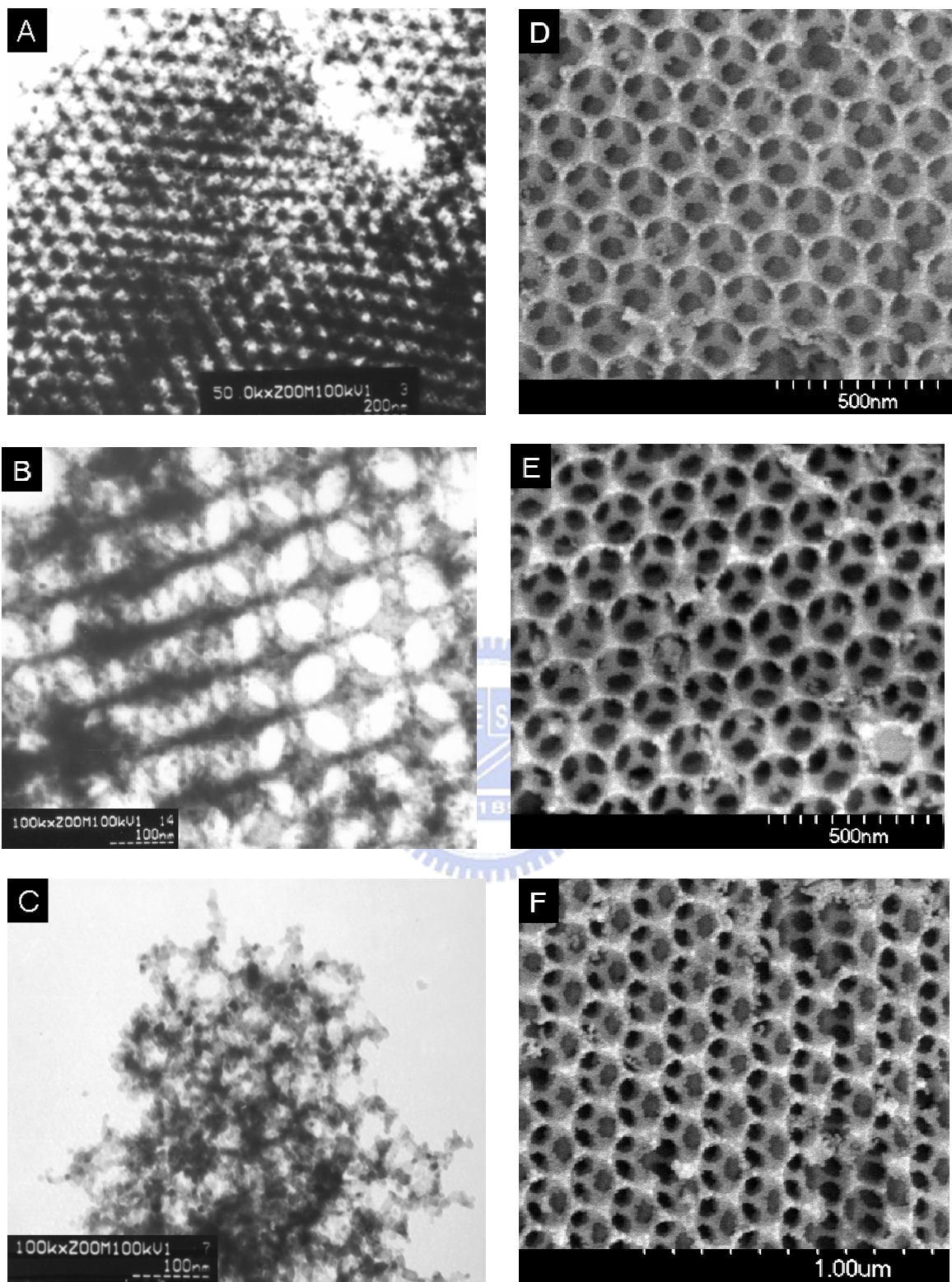


Figure 4-2 TEM (A~C) and SEM (D~F) micrographs of porous TiO_2 with different weight ratios of metal alkoxide/solvent of 0.2 (A, D), 0.6 (B, E) and 1.2 (C, F).

The bone-skin-like structure was obtained by coating titania films onto the ordered porous silica using surface sol-gel method. The preparation of porous silica is similar to that of porous TiO_2 . Figure 4-3 shows the TEM and SEM images of porous SiO_2 and bone-skin-like $\text{SiO}_2/\text{TiO}_2$. The SiO_2 also maintains ordered hexagonal porous structures in three dimensions. The wall thickness of porous SiO_2 is about 9.2 nm and observably thinner than that of porous TiO_2 . The pore diameter is about 170 nm indicating the 11 % shrinkage of the pore wall structure.

After coating TiO_2 on the surface of porous SiO_2 , the wall thickness ranged 13.9 to 18.6 nm was obtained. The thicker and uniform wall thicknesses of $\text{SiO}_2/\text{TiO}_2$ samples clearly indicate that the TiO_2 thin films are successfully coated onto the porous SiO_2 as bone-skin-like porous structures. The film thickness of sol-gel-derived TiO_2 increased from 4.6 to 9.4 nm when the TTIP/isopropanol weight ratios increased from 0.2 to 1.2. This result indicates that the concentration of precursor in the sol solution dominates the TiO_2 film thickness. Moreover, thinner films of TiO_2 can be formed using surface sol-gel method.

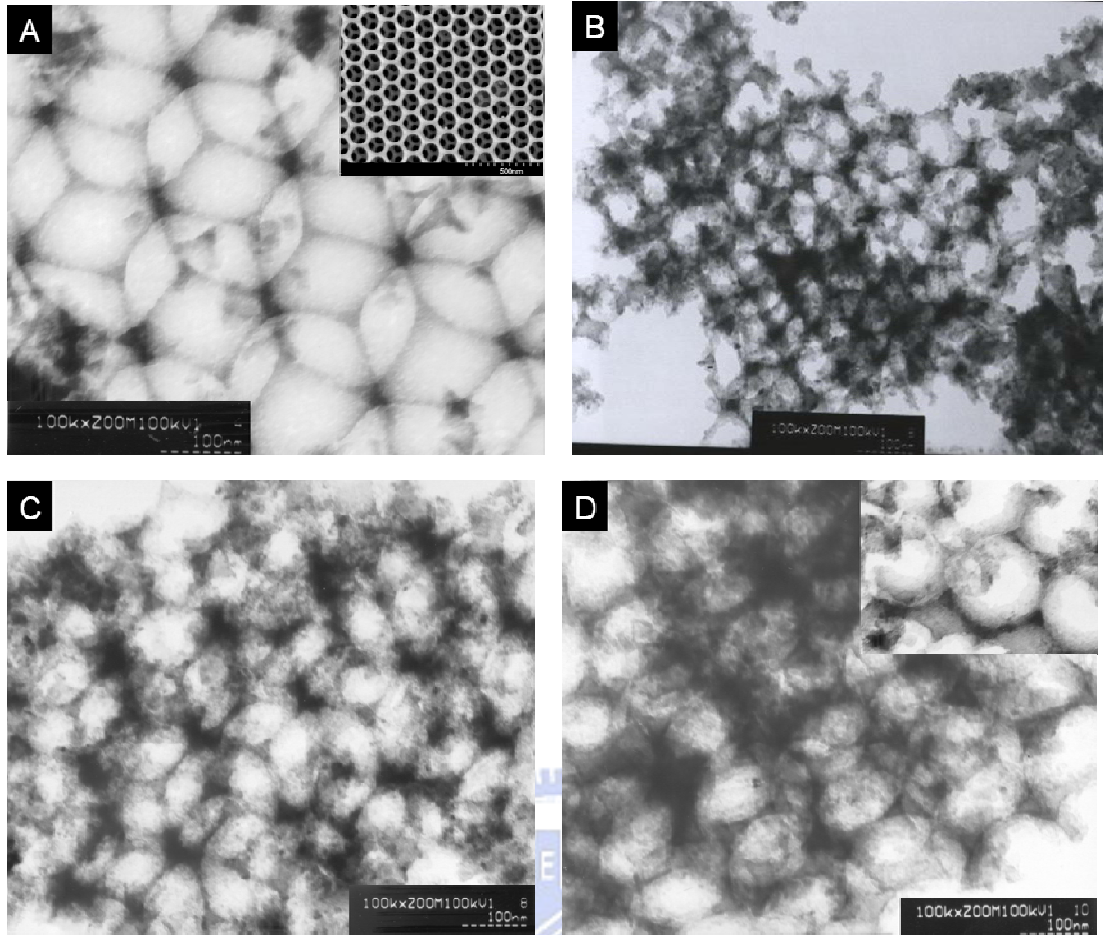


Figure 4-3 TEM images of porous SiO₂ (A) and bone-skin-like porous SiO₂/TiO₂ with weight ratios of alkoxide/solvent of 0.2 (B), 0.6 (C) and 1.2 (D). Insert in (A) shows the SEM image of porous SiO₂.

Table 4-1 Structural properties of various porous photocatalysts.

	Wall thickness (nm)	Average pore diameter (nm)	Shrinkage (%)	TiO ₂ film thickness ^a (nm)
TiO ₂ (0.2)	33.3	133.3	30	–
TiO ₂ (0.6)	35.2	141.7	25	–
TiO ₂ (1.2)	41.1	149.2	21	–
SiO ₂	9.2	170	11	–
SiO ₂ /TiO ₂ (0.2)	13.8	160.8	–	4.6
SiO ₂ /TiO ₂ (0.6)	17.0	154.4	–	7.8
SiO ₂ /TiO ₂ (1.2)	18.6	151.2	–	9.4

^aThe film thickness of sol-gel-derived TiO₂ were obtained from the increase of wall thickness of porous SiO₂/TiO₂ compare to that of porous SiO₂.

The bone-skin-like porous SiO₂/P-25 was also prepared to compare the physicochemical properties as well as photocatalytic activities with those of sol-gel-derived photocatalysts. Figure 4-4 shows the TEM images of porous SiO₂/P-25 samples. Numerous TiO₂ particles with large particle sizes were coated on the surface of porous SiO₂. In addition, the agglomeration of Degussa P-25 particles blocked the pores. The block was more serious at high concentration of Degussa P-25. This phenomenon leads to the decrease of surface area and pore volume of porous SiO₂/P-25 materials.

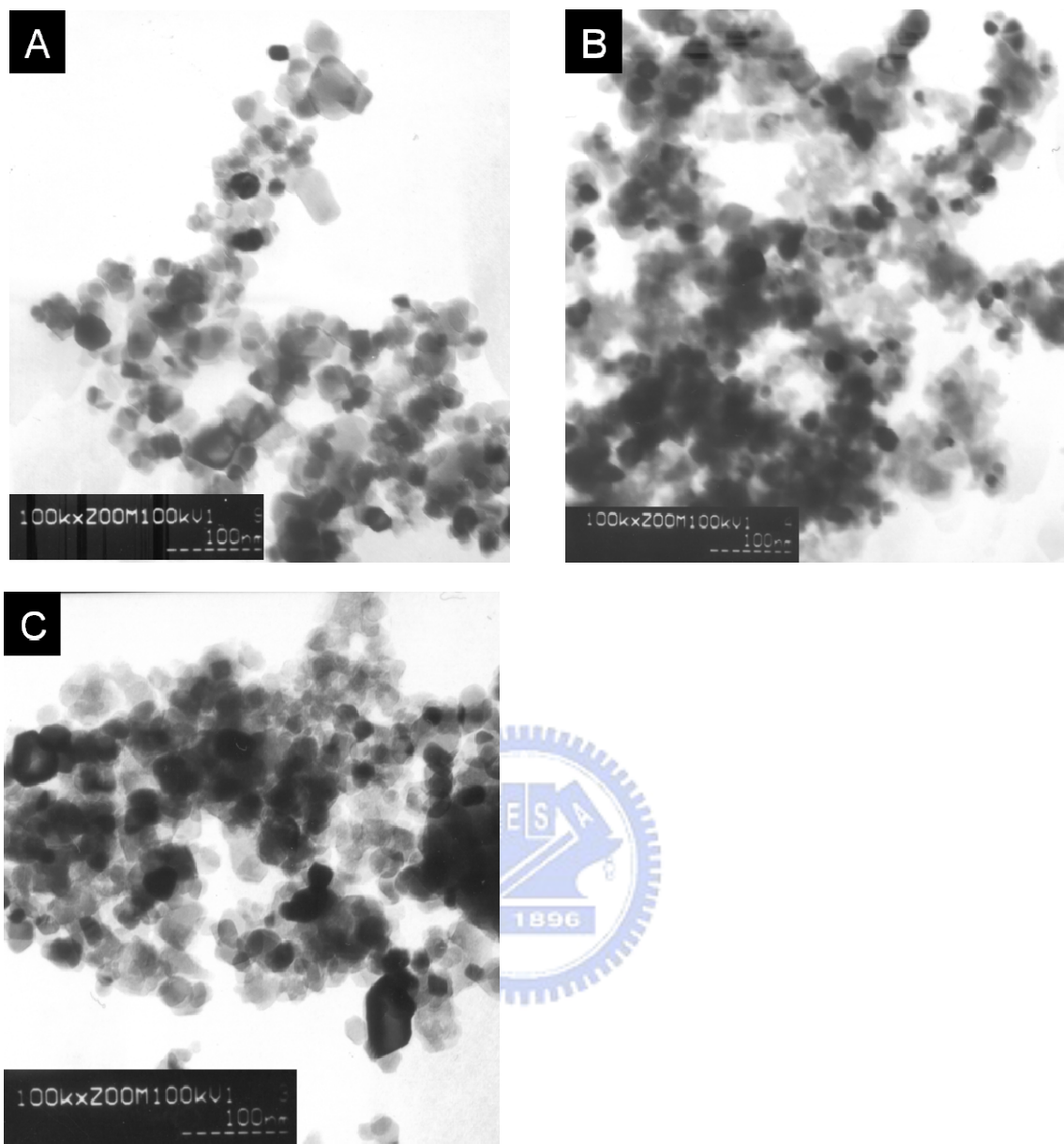


Figure 4-4 TEM images of bone-skin-like porous SiO₂/P-25 with different concentration about 0.2 (A), 0.6 (B) and 1.2 (C).

4.3 Textures of Porous TiO₂ and bone-skin-like SiO₂/TiO₂

The specific surface area and average pore size of all porous samples were determined by BET and BJH method. The specific surface area and average pore size of all porous samples were summarized in Table 4-2. All the isotherms of porous photocatalysts were listed in the appendix (Appendix B.).

Figure 4-5 shows the nitrogen adsorption-desorption isotherm of porous TiO₂ with the precursor concentration of 0.6. According to the IUPAC classification(site), the isotherms of porous TiO₂ were showed the Type II behaviors indicating the adsorption on macroporous structures with strong adsorbate-adsorbent interactions. The surface areas of porous TiO₂ samples decreased from 79.4 to 64.9 m²/g with increasing precursor concentrations. The result indicates that the loss of structural ordering accompanied with the decreasing surface area for the porous TiO₂ with high precursor concentration. The surface areas of porous TiO₂ samples were remarkable lower than porous SiO₂ (507.9 m²/g) and bone-skin-like porous photocatalysts due to their thick wall thicknesses.

Figure 4-6 shows the nitrogen adsorption-desorption isotherm and corresponding BJH pore-size distribution curves of porous SiO₂/TiO₂ with the precursor concentration of 0.6. This isotherm showed the Type IV behaviors indicating the mesoporous and macroporous structures of these porous samples.(siteB3.7) The mesoporous structure was resulted from the sol-gel-derived TiO₂ and the macroporous structure corresponded to the ordered hexagonal porous structures in three dimensions. A hysteresis loop at high relative pressure could be observed, which is due to the capillary condensation relative with mesopores(siteZ). This isotherm exhibit stepwise adsorption and desorption which is indicative of three-dimensional intersection of porous structure^{23,24}. All the porous SiO₂/TiO₂ samples have high specific surface areas (410.5 ~ 534.9 m²/g) and pore volumes (0.34 ~ 0.42 cm³/g). It is noticed that the surface area of porous SiO₂/TiO₂ with the precursor concentration of 0.2 was 534.9 m²/g and larger than that of porous SiO₂. The large surface area resulted from the

macroporous structure of porous SiO₂ and the mesoporous structure of sol-gel-derived TiO₂ films coating onto the silica. The surface area of porous SiO₂/TiO₂ also decreased with increasing precursor concentration. This phenomenon was due to the thicker TiO₂ film formed at higher precursor concentration corresponded to the increasing entire weights of porous SiO₂/TiO₂ samples.

Figure 4-7 showed the nitrogen adsorption-desorption isotherm of porous SiO₂/P-25 with the TiO₂ concentration of 0.6. This isotherm also showed the Type IV behaviors with an adsorption-desorption hysteresis at high relative pressure. However, the isotherm raised rapidly near zero pressure indicating that the samples contain micropores(siteB125). This feature could be also observed in the isotherm of SiO₂, but absence in those of porous SiO₂/TiO₂. The result indicates the incomplete coating of P25 on the surface of porous SiO₂. The surface areas of porous SiO₂/P-25 were much lower than that of porous SiO₂/TiO₂. The result indicates that large TiO₂ particles coated onto the porous SiO₂ and resulted in the agglomeration of Degussa P-25 particles blocked the pores. The surface areas of porous SiO₂/P-25 decreased from 290.2 to 140.3 m²/g with the increasing TiO₂ concentrations due to the more serious blockages at high concentration of Degussa P-25. The phenomenon can be also confirmed by the TEM images.

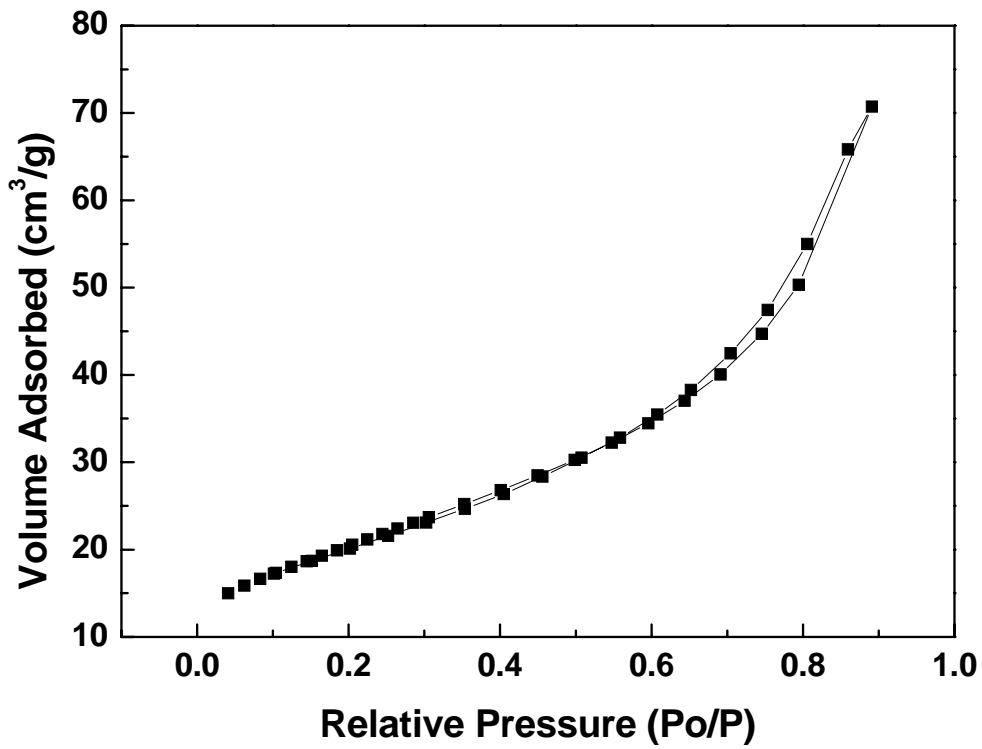


Figure 4-5 Nitrogen adsorption-desorption isotherm of porous TiO₂ with the precursor concentration of 0.6.

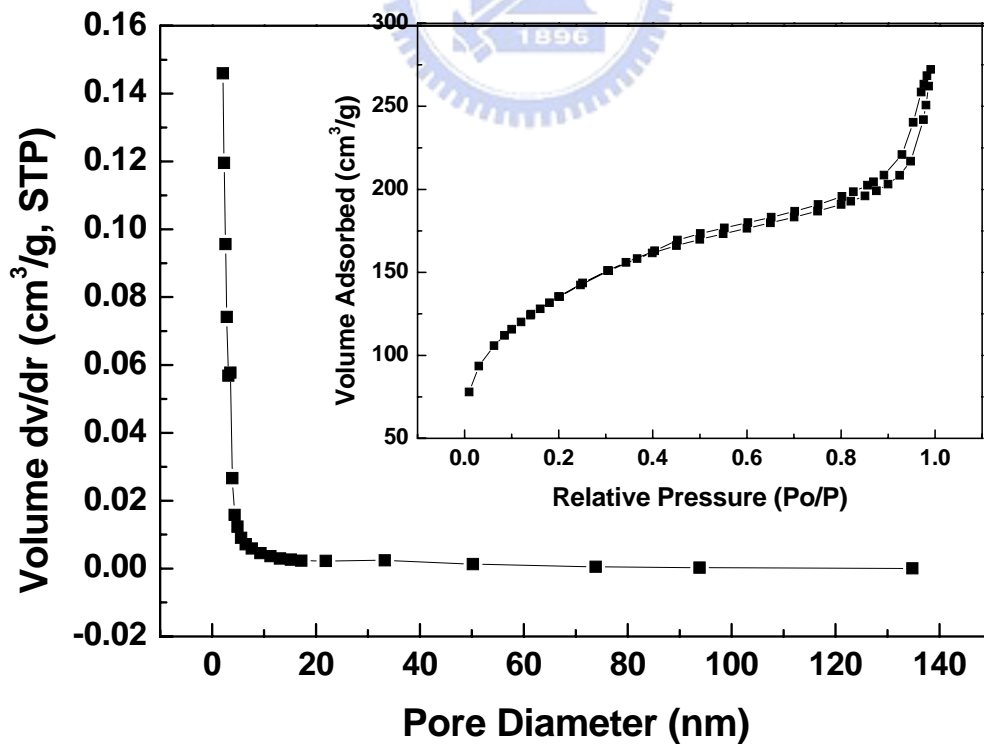


Figure 4-6 Nitrogen adsorption-desorption isotherms (inset) and corresponding BJH pore-size distribution curves of porous SiO₂/TiO₂ with precursor concentration of 0.6.

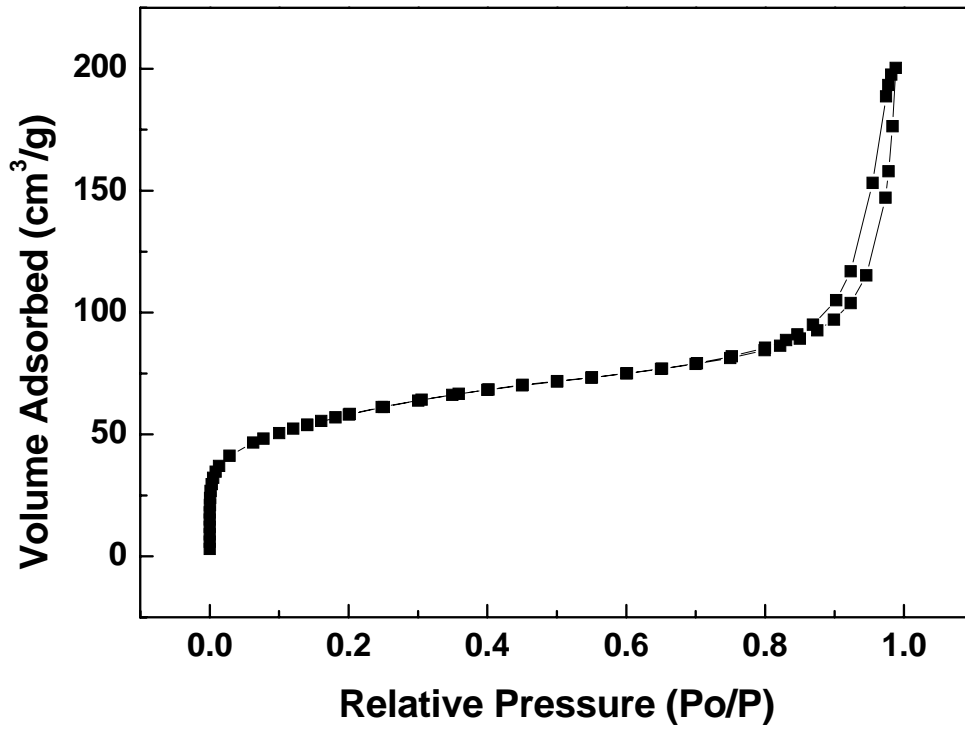


Figure 4-7 Nitrogen adsorption-desorption isotherm of porous SiO₂/P-25 with the TiO₂ concentration of 0.6.

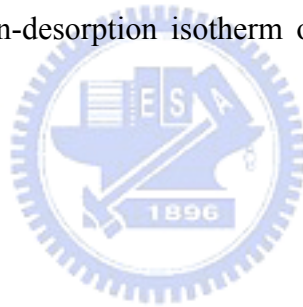


Table 4-2 Pore-wall properties of porous TiO₂ and bone-skin-like SiO₂/TiO₂ with various weight ratios of alkoxide/solvent.

Samples	BET area (m²/g)	Average pore diameter (nm)	Pore volume (cm³/g)
TiO ₂ (0.2)	79.4	2.8	0.11
TiO ₂ (0.6)	73.3	3.0	0.12
TiO ₂ (1.2)	64.9	3.6	0.11
SiO ₂	507.9	6.6	0.38
SiO ₂ /TiO ₂ (0.2)	534.9	3.0	0.42
SiO ₂ /TiO ₂ (0.6)	470.1	3.1	0.37
SiO ₂ /TiO ₂ (1.2)	410.5	3.2	0.34
SiO ₂ /P-25(0.2)	290.2	7.2	0.26
SiO ₂ /P-25(0.6)	202.9	9.0	0.23
SiO ₂ /P-25(1.2)	142.3	12.7	0.22

4.4 Crystalline properties of Porous TiO₂ and bone-skin-like SiO₂/TiO₂

Calcination not only removes the PS templates, but also crystallizes the TiO₂. The crystalline properties of the porous TiO₂ and bone-skin-like SiO₂/TiO₂ were examined by XRD. Figure 4-6 shows the XRD patterns of porous TiO₂ with different metal alkoxide/solvent weight ratios. Pure anatase form was obtained in all the porous TiO₂ calcined at 500 °C. The crystallite sizes of all samples were calculated from the broadening of the deflection peaks using Schererr equation and the results were summarized in Table 4-3. The crystallite sizes of the porous TiO₂ samples increased from 9.3 to 10.8 nm as the weight ratio increased from 0.2 to 1.2. The crystallite sizes were smaller than the wall thickness of the TiO₂ (42 ~ 58 nm), indicating that the porous TiO₂ is polymorph.

Figure 4-7 shows the XRD patterns of porous SiO₂ and bone-skin-like SiO₂/TiO₂. The sol-gel-derived porous silica was amorphous after calcinations at 500 °C. All the bone-skin-like structures exhibited anatase form. The crystallite sizes of bone-skin-like SiO₂/TiO₂ samples increased from 4.6 to 8.7 nm as the weight ratio increased from 0.2 to 1.2. The crystallite sizes were similar with the film thickness of the TiO₂ observed from the TEM images (4.6 ~ 9.4 nm).

Figure 4-8 shows the XRD patterns of porous SiO₂/P-25 samples prepared by different TiO₂ loading in slurry. All the bone-skin-like SiO₂/P-25 samples show the main anatase phase and minor rutile phase. When the TiO₂ concentration was 1.2, the XRD pattern of SiO₂/P-25 exhibited more remarkable amorphous effect around 20° 2θ than those obtained from 0.6 and 0.2. This phenomenon depicts that the P-25 TiO₂ was sufficiently coated onto the porous SiO₂ at high concentration due to agglomeration. The poor coating is also observed in TEM images. Therefore, the resulting porous SiO₂/P-25 powders with slurry concentration about 1.2 is probably consist of some porous SiO₂ 、 agglomeration of Degussa P-25 particles and few bone-skin-like structures.

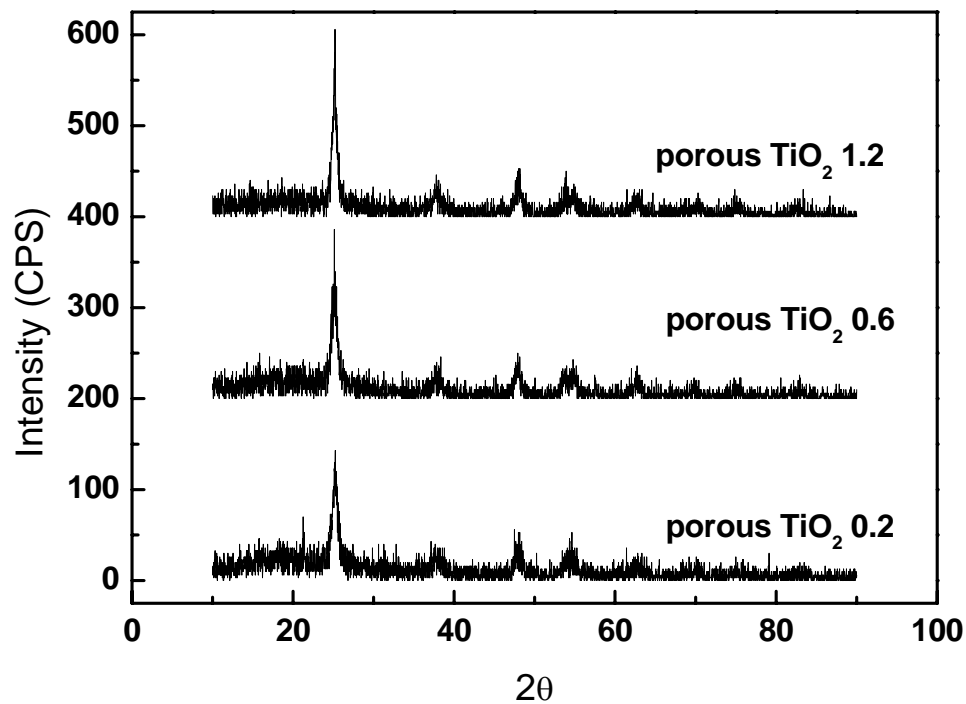


Figure 4-8 XRD patterns of porous TiO₂ with various weight ratios of alkoxide/solvent.

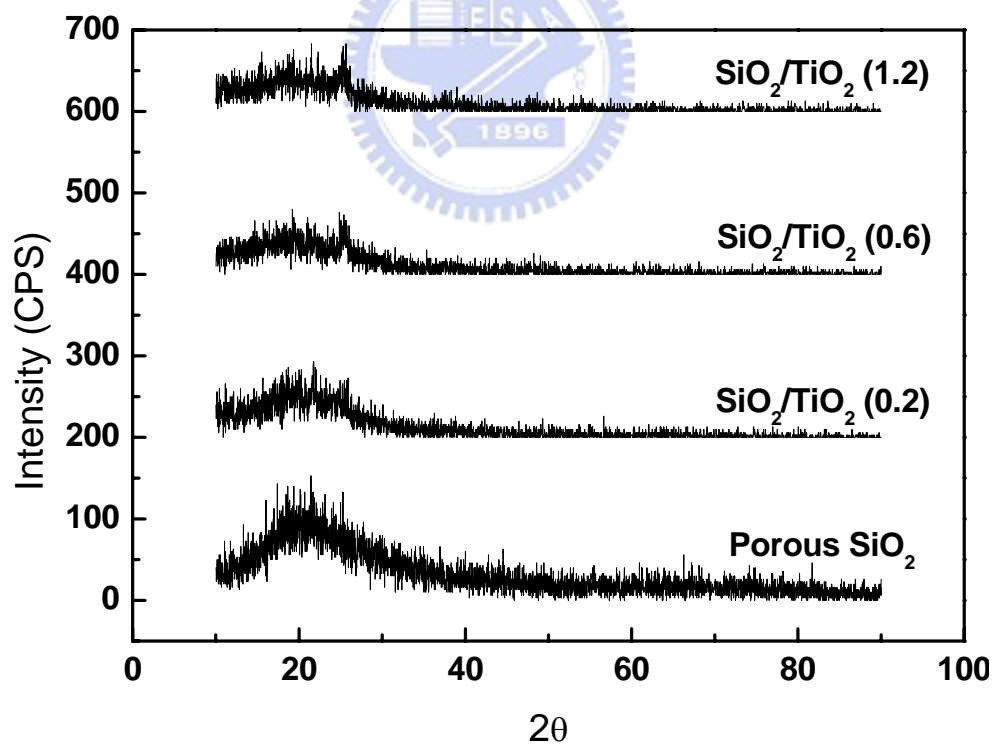


Figure 4-9 XRD patterns of bone-skin-like porous SiO₂/TiO₂ with various weight ratios of TTIP/solvent and porous SiO₂.

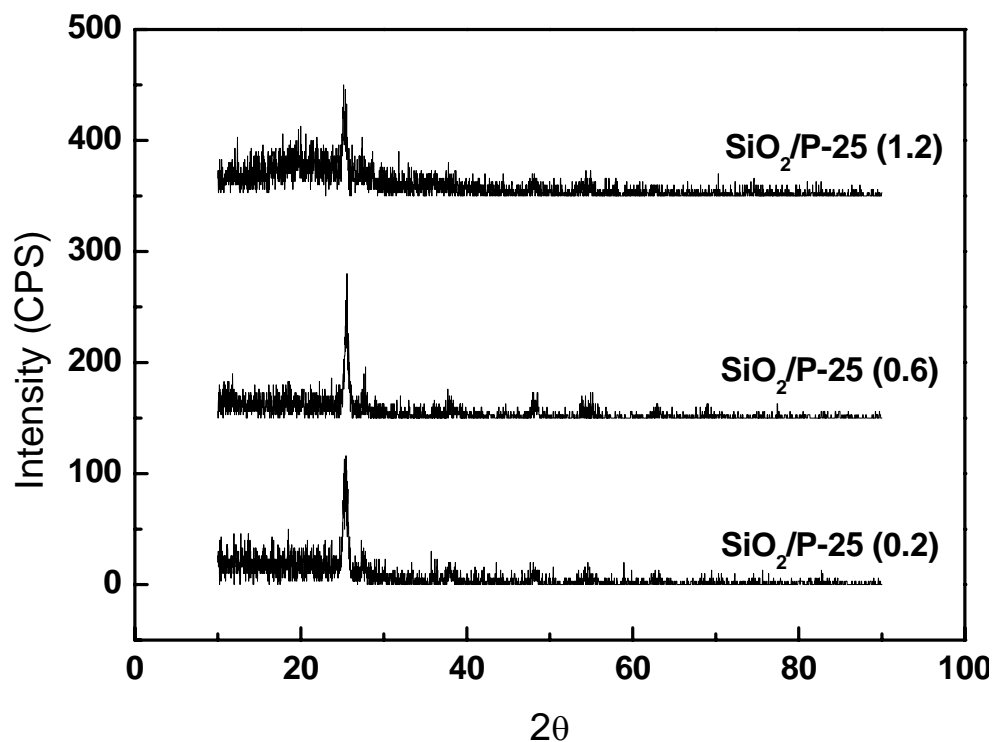


Figure 4-10 XRD patterns of bone-skin-like porous $\text{SiO}_2/\text{P-25}$ with various slurry concentrations.

Table 4-3 Crystalline sizes of porous TiO_2 and $\text{SiO}_2/\text{TiO}_2$ with various weight ratios of alkoxide/solvent

Samples	Crystallite size (nm)
TiO_2 (0.2)	9.3
TiO_2 (0.6)	9.8
TiO_2 (1.2)	10.8
$\text{SiO}_2/\text{TiO}_2$ (0.2)	4.6
$\text{SiO}_2/\text{TiO}_2$ (0.6)	7.8
$\text{SiO}_2/\text{TiO}_2$ (1.2)	8.7

Figure 4-9 shows the HRTEM images of bone-skin-like $\text{SiO}_2/\text{TiO}_2$ prepared by different TTIP/isopropanol weight ratios and the HRTEM images of porous $\text{SiO}_2/\text{P-25}$ with dilution of 0.6. The HRTEM images (arrowed sections) show that crystallite sizes range from 4.00 to 9.06 nm which are close to those obtained from XRD. Moreover, the crystallite sizes are similar to the film thickness observed from TEM images, indicating that the nanocrystals in the surface sol-gel coated films grow preferentially along anatase (101) plane that is parallel to SiO_2 substrate. The coated films are constructed by P-25 TiO_2 particles. Each particle is high crystalline with large crystallite sizes (23.8 nm). The large particle sizes and the polycrystalline properties would affect the further photocatalytic activities of porous $\text{SiO}_2/\text{P-25}$ samples.



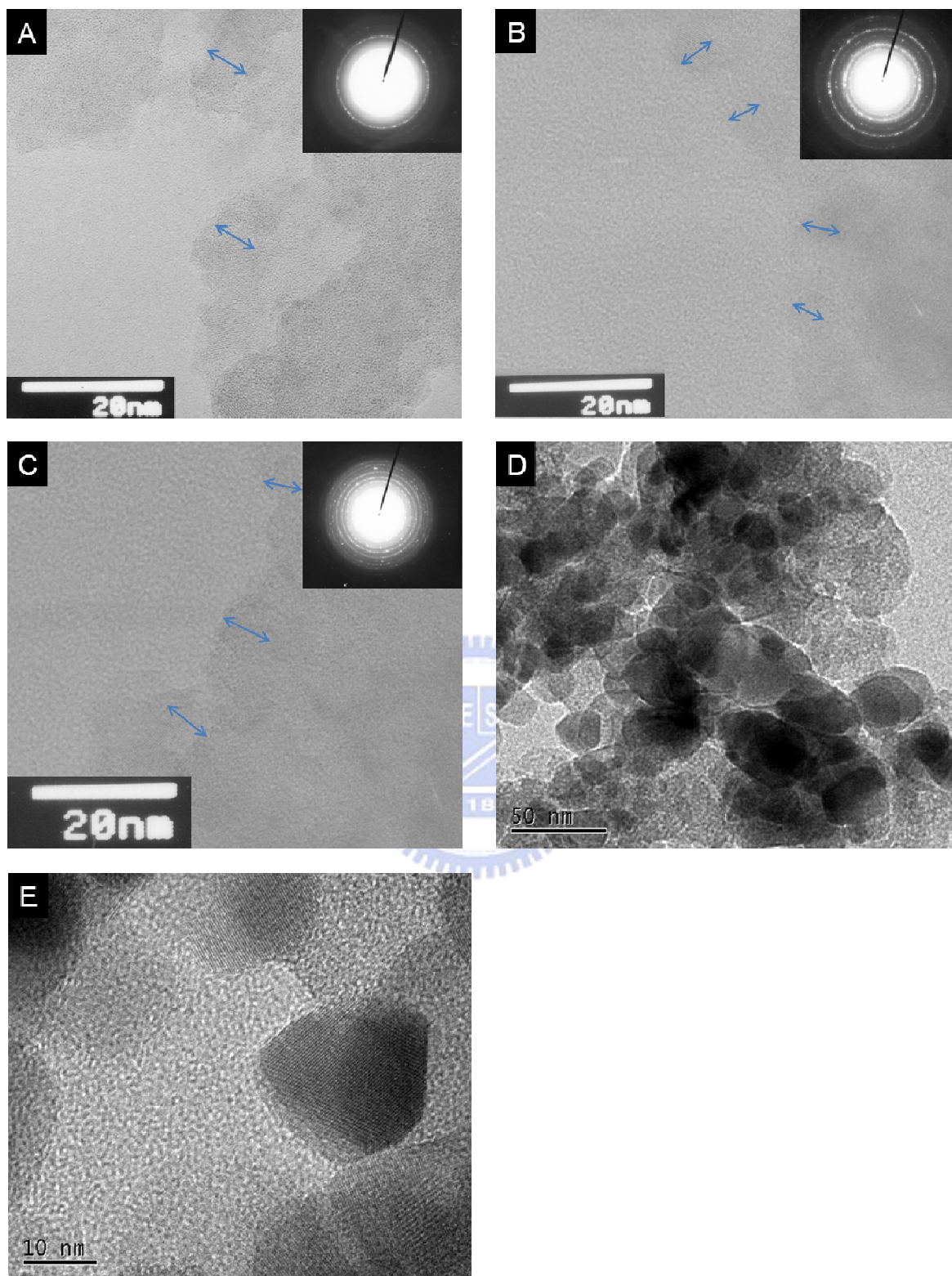


Figure 4-11 HRTEM images of bone-skin-like porous $\text{SiO}_2/\text{TiO}_2$ with various precursor concentrations of 0.2 (A), 0.6 (B) and 1.2 (C) and porous $\text{SiO}_2/\text{P-25}$ with TiO_2 concentration of 0.6 (D,E).

4.5 Optical properties of Porous TiO₂ and bone-skin-like SiO₂/TiO₂

The optical properties of all porous photocatalysts were measured by the UV-Vis spectra. Figure 4-10 ~ 12 show the UV/vis absorption spectra of porous TiO₂, bone-skin-like SiO₂/TiO₂ and SiO₂/P-25, respectively. The band gap energies of all porous samples calculated from the adsorption edge were shown in Table 4-4. The band gap energies of these porous photocatalysts were similar and about 3.5 eV. The result indicates the all the porous photocatalysts with small crystallite sizes showed the quantum size effects²⁵. This was also confirmed by their larger band gap energies than that of bulk TiO₂ phase (E_g = 3.0 to 3.2 eV). Although the band gap energies of these porous photocatalysts were similar, the absorption edges of porous SiO₂/P-25 were more widen than that of porous TiO₂ and SiO₂/TiO₂. The absorption edge of semiconductors may vary with crystal size, lattice strain or disordering and amorphization. More quantities of plane defects in grain boundaries may widen the absorption edge²⁶. The result indicates that the porous SiO₂/P-25 samples had the polymorph structures resulting in the more grain boundaries. The shaper absorption edges of porous SiO₂/TiO₂ also corresponded to the low amounts of bulk defects. Those results can be confirmed with the HRTEM images.

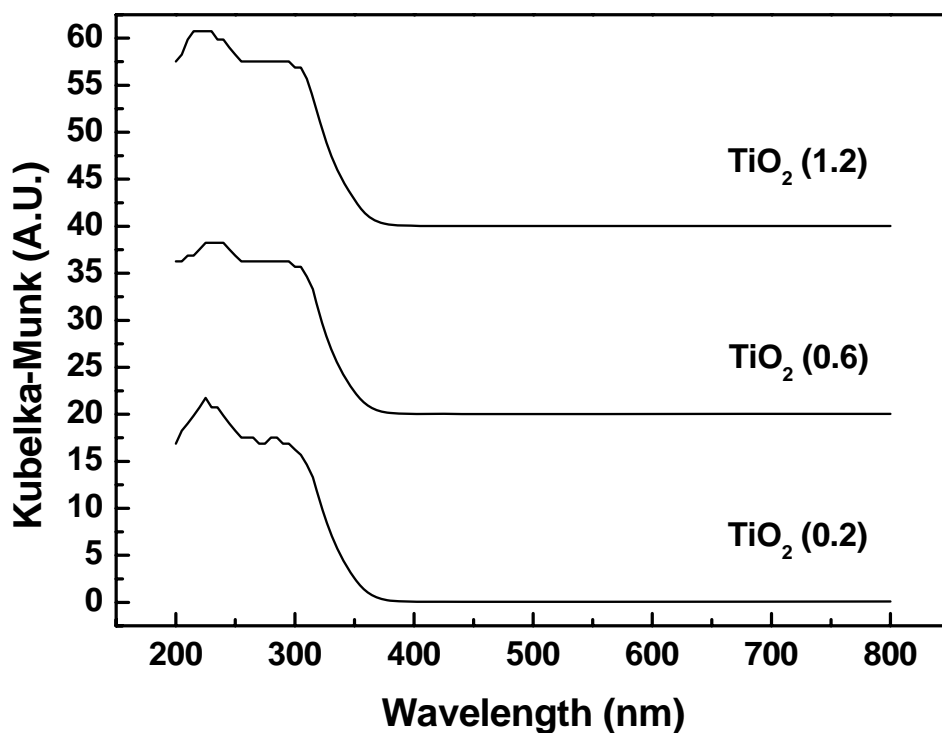


Figure 4-12 UV-Vis spectra shows the optical properties of the porous TiO₂ with different metal alkoxide/solvent weight ratios.

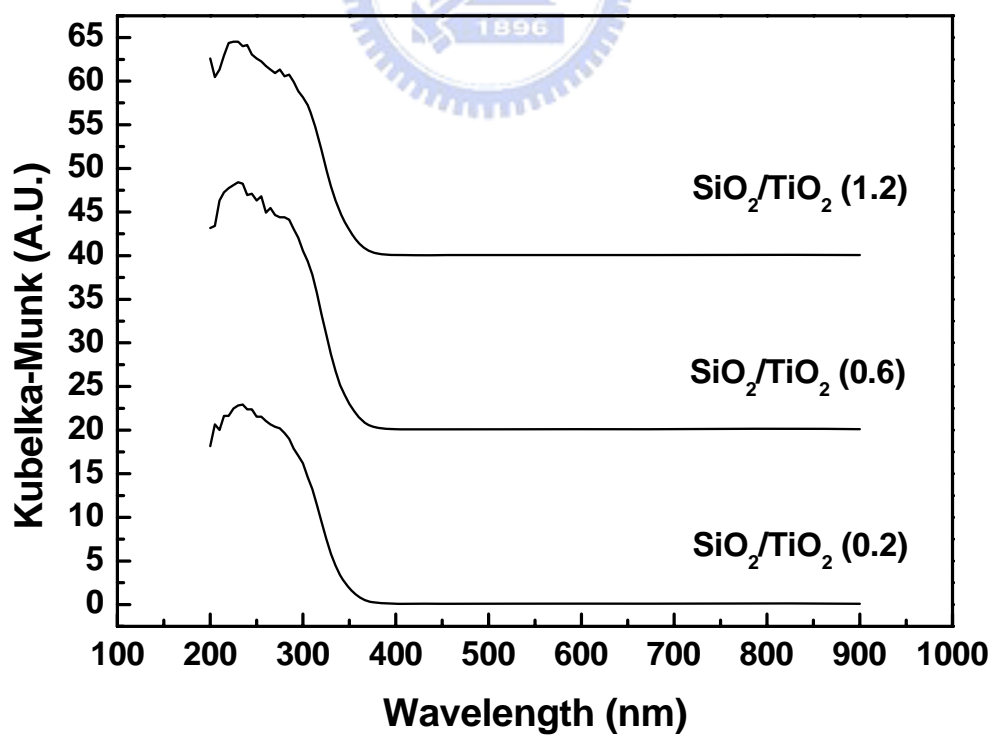


Figure 4-13 UV-Vis spectra shows the optical properties of the porous SiO₂/TiO₂ with different metal alkoxide/solvent weight ratios.

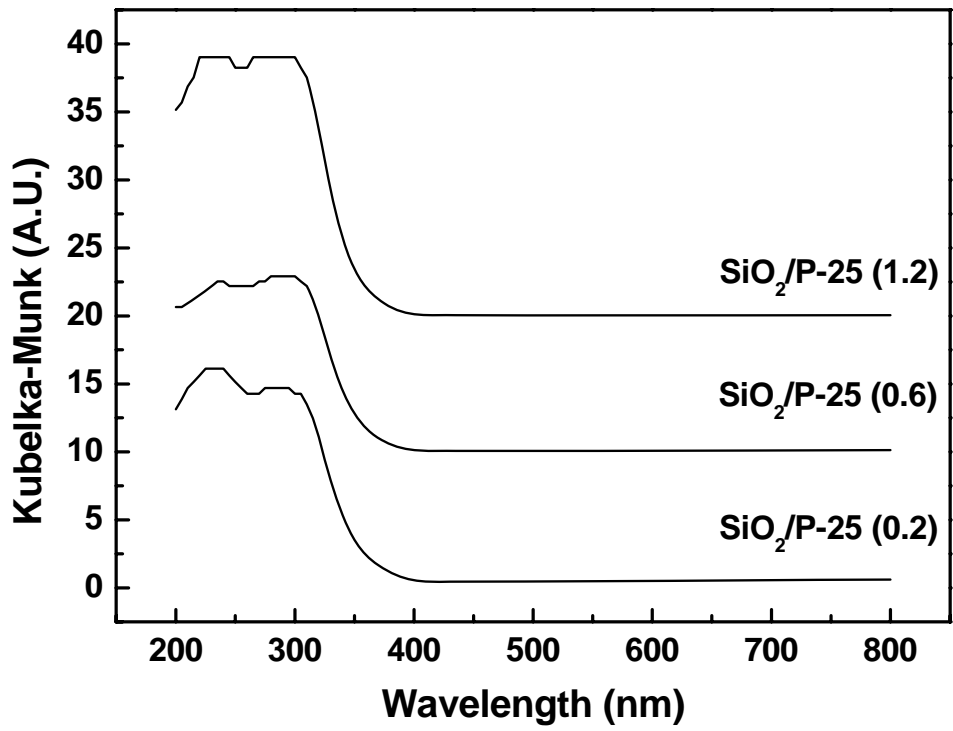
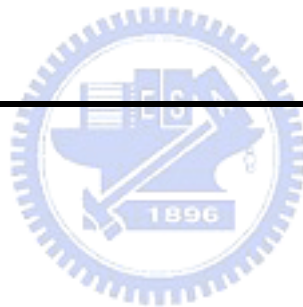


Figure 4-14 UV-Vis spectras of the bone-skin-like porous SiO₂/P-25 with various slurry concentrations.



Table 4-4 The band gap energies of all porous samples.

Samples	Bandgap (eV)
TiO ₂ (0.2)	3.5
TiO ₂ (0.6)	3.5
TiO ₂ (1.2)	3.4
SiO ₂ /TiO ₂ (0.2)	3.5
SiO ₂ /TiO ₂ (0.6)	3.5
SiO ₂ /TiO ₂ (1.2)	3.5
SiO ₂ /P-25(0.2)	3.4
SiO ₂ /P-25(0.6)	3.4
SiO ₂ /P-25(1.2)	3.5



4.6 EPR studies of Porous TiO₂ and bone-skin-like SiO₂/TiO₂

In the process of photocatalysis, the photoinduced electrons and holes will be trapped at the surface of photocatalyst and form the paramagnetic species. These radicals can react with the reactant molecules adsorbed on the surface of photocatalysts and be detected by electron spin resonance spectroscopy. All the signals observed in the spectra were characterized by the sets of g values. EPR parameters and the assignments of all signals obtained in this study were summarized in Table 4-5. The intensities of all signals were obtained from the integrations of the spectra and were summarized in Table 4-6.

Figure 4-15 shows the EPR spectra of porous TiO₂ with various precursor concentrations measured at 77 K under UV irradiation. Two mainly features which were labeled as signal A and B can be observed in the spectra. The signal A was characterized with parameters $g_1 = 2.024$, $g_2 = 2.009$, and $g_3 = 2.003$. It was ascribed to the surface Ti⁴⁺–O₂⁻ species which were formed on anatase after UV irradiation and O₂ adsorption. The oxygen adsorbed on the surface of porous TiO₂ were trapped the photogenerated electrons to form this species. After integrating the spectra of porous TiO₂ samples, the intensities of signals A and B were shown in Table 4-6. The intensity of signal A decreased with increasing precursor concentration. It was due to the reduction of surface area and the resulting less amount of adsorbed O₂ at high precursor concentration. The signal B was characterized with parameters $g_1 = 1.961$, $g_2 = 1.992$, and $g_3 = 1.992$. The radicals of signal B were assigned to the inner Ti³⁺ species, which were formed when the titanium atoms inside the particles trapped photogenerated electrons.(site) The inner Ti³⁺ species can not participate in the surface reactions and act as charge recombination centers which may reduce the photocatalytic activities of photocatalysts.

Figure 4-16 shows the EPR spectra of porous SiO₂/TiO₂ with various precursor concentrations measured at 77 K under UV irradiation. All the porous SiO₂/TiO₂ samples showed the same feature which was signal C with $g_1 = 2.024$, $g_2 = 2.013$, and $g_3 = 2.003$.

This signal was assigned to the $\text{Ti}^{4+}-\text{O}^- - \text{Ti}^{4+}-\text{OH}^-$ species which were formed after UV irradiation of hydroxylated TiO_2 . The surface hydroxyl groups or oxygen atoms in the crystalline lattice near the surface of TiO_2 will trap the photoinduced holes to form the $\text{Ti}^{4+}-\text{O}^- - \text{Ti}^{4+}-\text{OH}^-$ species. However, an additional feature can be observed in the spectrum of porous $\text{SiO}_2/\text{TiO}_2$ with the precursor concentration of 0.2. This feature labeled as signal D was characterized by the sets of g values, $g_1 = 1.957$, $g_2 = 1.990$, and $g_3 = 1.990$. It was reported to the surface Ti^{3+} species which were formed from the titanium atoms on the surface trapping the photogenerated electrons. The intensities of these spectra increased with increasing precursor concentrations. It is the result of thicker sol-gel-derived TiO_2 film obtained at high precursor concentration.

Figure 4-17 shows the EPR spectra of porous $\text{SiO}_2/\text{P-25}$ with various TiO_2 concentrations measured at 77 K under UV irradiation. These spectra also exhibited the signal C and the porous $\text{SiO}_2/\text{P-25}$ with TiO_2 concentration of 1.2 had the lowest intensity of signal C. This was attributed to the lowest surface area of porous $\text{SiO}_2/\text{P-25}$ with TiO_2 concentration of 1.2 following by the less amounts of surface hydroxyl groups than that of other $\text{SiO}_2/\text{P-25}$ samples.

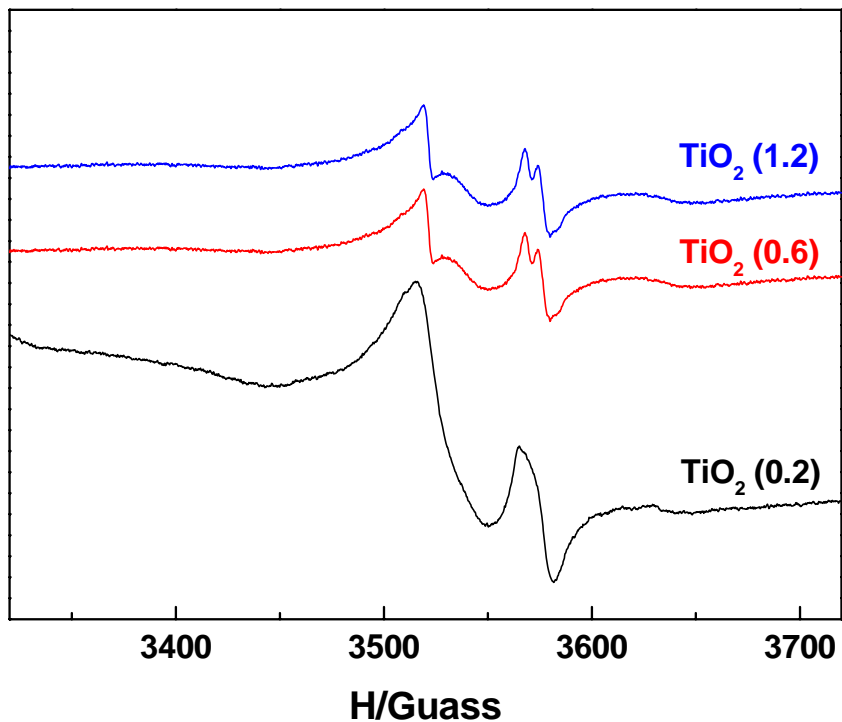


Figure 4-15 EPR spectra of porous TiO_2 with various precursor concentrations measured at 77 K under UV irradiation.

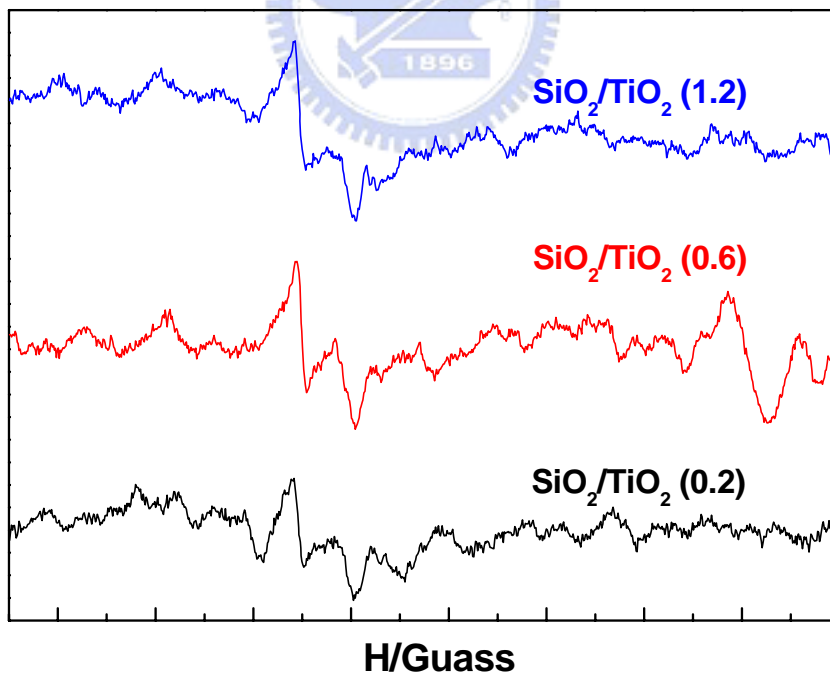


Figure 4-16 EPR spectra of porous $\text{SiO}_2/\text{TiO}_2$ with various precursor concentrations measured at 77 K under UV irradiation.

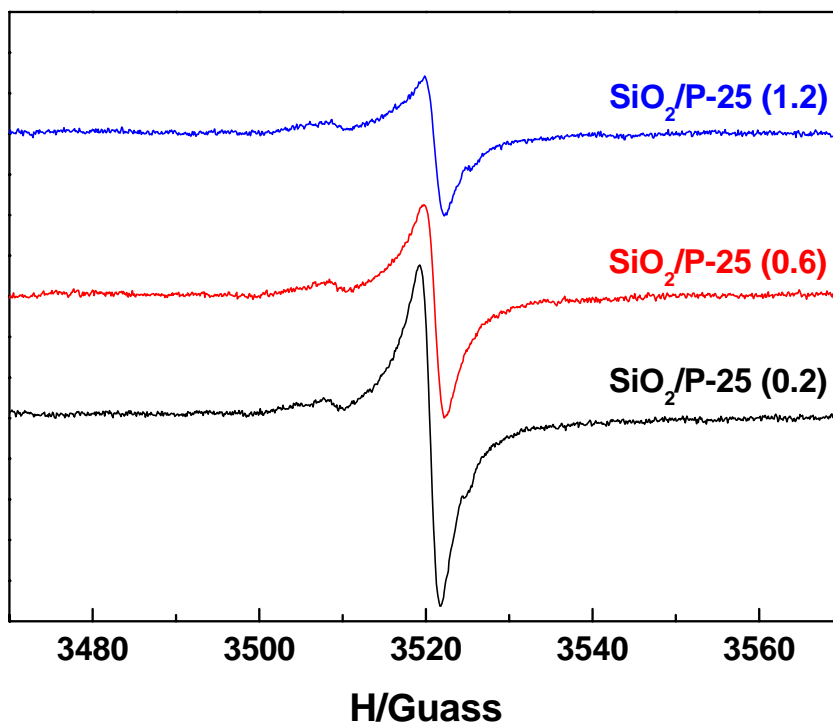


Figure 4-17 EPR spectra of porous SiO₂/P-25 with various TiO₂ concentrations measured at 77 K under UV irradiation.

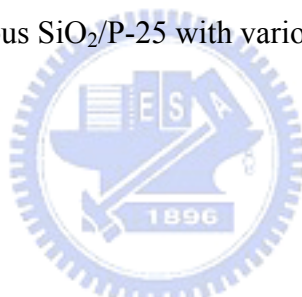


Table 4-5 Summary of EPR parameters and the assignments of the signals obtained in this study.

Signal	EPR parameters			Assignment
	g1	g2	g3	
A	2.024	2.009	2.003	Ti ⁴⁺ —O ₂ ⁻ on anatase
B	1.957	1.992	1.992	Inner Ti ³⁺
C	2.024	2.013	2.003	Ti ⁴⁺ —O ⁻ —Ti ⁴⁺ —OH ⁻
D	1.957	1.990	1.990	Surface Ti ³⁺

Table 4-6 The intensities of all signals obtained from the integrations of the spectra.

Samples	Signal	Intensity
Porous TiO ₂ (0.2)	A	1.8×10 ⁶
	B	1.5×10 ⁶
Porous TiO ₂ (0.6)	A	4.4×10 ⁵
	B	3.9×10 ⁵
Porous TiO ₂ (1.2)	A	3.0×10 ⁵
	B	2.4×10 ⁵
Porous SiO ₂ /TiO ₂ (0.2)	C	2.9×10 ⁴
Porous SiO ₂ /TiO ₂ (0.6)	C	2.0×10 ⁴
	D	2.3×10 ⁴
Porous SiO ₂ /TiO ₂ (1.2)	C	8.0×10 ⁴
Porous SiO ₂ /P-25 (0.2)	C	1.1×10 ⁵
Porous SiO ₂ /P-25 (0.6)	C	6.5×10 ⁴
Porous SiO ₂ /P-25 (1.2)	C	4.7×10 ⁴

4.7 Photoactivities- Degradation of Rhodamine B

To understand the effect of different porous structures on the photocatalytic activities of photocatalysts, the degradation of Rhodamine B with the initial concentration about 0.05 mM ($C_0 = 0.05$ mM) was examined. Figure 4-16 shows the photodegradation of RhB by porous TiO_2 prepared by different alkoxide/ solvent weight ratios. The decoloration of Rh B can be completed within 30 minutes for each case. Moreover, all the degradation reactions follow pseudo-first order kinetics. Table 4-7 summarizes the rate constants and the rate constants normalized with mass or specific surface area of the porous photocatalysts. The porous TiO_2 at the precursor concentration of 0.6 performed the highest photocatalytic activity with a rate constant of $3.0 \times 10^{-1} \text{ min}^{-1}$. The following is by the weight ratio of 1.2 that showed a rate constant of $2.7 \times 10^{-1} \text{ min}^{-1}$. The weight ratio of 0.2 exhibited the slowest reaction kinetics with a rate constant of $1.1 \times 10^{-1} \text{ min}^{-1}$. The reaction rate increases with increasing alkoxide/ solvent weight ratios as the ratio below 0.6. Since the thick wall thickness was obtained at high precursor concentration, the high reactivity is due to that more active charges are produced by thick wall thickness so as improve the photoefficiency²⁷. The weight ratio of 1.2 resulted in the thickest wall thickness. However, the poorer photoactivity was obtained compared to that porous TiO_2 at weight ratio of 0.6. It is attributed to the loss of structural ordering accompanied with the decreasing surface area for the porous TiO_2 with high precursor concentration.

Figure 4-17 shows the photodegradation of RhB by bone-skin-like $\text{SiO}_2/\text{TiO}_2$ prepared by different alkoxide/ solvent ratios. The decoloration of Rh B can be completed within 35 minutes. The porous TiO_2 at the precursor concentration of 1.2 performed the highest photocatalytic activity with a rate constant of $1.3 \times 10^{-1} \text{ min}^{-1}$. The following is by the weight ratio of 0.6 that showed a similar rate constant of $1.2 \times 10^{-1} \text{ min}^{-1}$. The weight ratio of 0.2 exhibited the slowest reaction kinetics with a rate constant of $8.3 \times 10^{-2} \text{ min}^{-1}$. The reaction rate increases with increasing alkoxide/ solvent weight ratios. It should be noted

that the bone-skin-like structures contained less amount of TiO₂ than pure porous TiO₂ when adding the same amount of photocatalysts into the Rhodamine B solution. Therefore, the rate constants of the porous photocatalysts were further normalized by their real content of TiO₂ to get the specific photoactivities. The real mass of titania of bone-skin-like structure was measured by the ICP-MS. Table 4-6 lists the Si/Ti weight percentages of the bone-skin-like porous photocatalysts and the mass of titania in every 15 mg of bone-skin-like photocatalysts. The real mass of coated titania increased from 2.3 to 4.5 mg with increasing precursor concentration when sol-gel method was adapted. Much higher contents of TiO₂ (7.6 ~ 11.5 mg) were obtained in SiO₂/P-25. This result is primarily due to the agglomeration of Degussa P-25 particles. After normalization of the rate constants with TiO₂ contents, the porous sol-gel-derived TiO₂ film at the precursor concentration of 0.2 showed the highest specific photocatalytic activity of $3.6 \times 10^{-2} \text{ min}^{-1} \text{ mg}^{-1}$. The specific photocatalytic activity decreased slightly with increasing alkoxide/ solvent weight ratios and the lowest photocatalytic activity ($2.9 \times 10^{-2} \text{ min}^{-1} \text{ mg}^{-1}$) took place at weight ratio of 1.2. This result is attribute to that low surface area is resulted at high precursor concentrations. In addition, the TiO₂ film thickness increased with the precursor concentrations. The weight ratio of 0.2 results in the thinnest TiO₂ film (thickness is 4.6 nm), thus short charge diffusion length is beneficial for high photocatalytic activity²⁸.

Figure 4-18 shows the photodegradation of RhB by bone-skin-like SiO₂/P-25 prepared by different P-25/ solvent weight ratios. The decoloration of Rh B can be completed within 25 minutes. The photoactivities of the P-25 TiO₂ films are ranked in the order as 1.2 ($3.1 \times 10^{-1} \text{ min}^{-1}$) > 0.6 ($2.9 \times 10^{-1} \text{ min}^{-1}$) > 0.2 ($2.6 \times 10^{-1} \text{ min}^{-1}$) P-25/solvent weight ratio. The reaction rate also increased with increasing P-25/ solvent weight ratio due to the more amount of Degussa P-25. However, the specific photocatalytic activity of P-25 TiO₂ film displayed the opposite train upon TiO₂ concentration in coating solutions. The weight ratio of 0.2 had highest specific photocatalytic activity of $3.4 \times 10^{-2} \text{ min}^{-1} \text{ mg}^{-1}$ over that of 0.6 (3.0×10^{-2}

$\text{min}^{-1}\text{mg}^{-1}$) and 1.2 ($2.7 \times 10^{-2} \text{ min}^{-1}\text{mg}^{-1}$). This phenomenon is as the consequence of low surface area resulted from serious blocking of pores by P-25 TiO_2 at high TiO_2 concentration.

Apparently, the degradation rate constants of sol-gel-derived TiO_2 films were lower than that of porous TiO_2 and Degussa P-25 films. However, they exhibited the highest specific photocatalytic activities over the other two kinds of photocatalysts. The special high photoactivities of the sol-gel-derived TiO_2 films are associated with low amounts of bulk defects. In porous TiO_2 and P-25 TiO_2 films, the polymorph structure contents high quantities of plane defects in grain boundaries. The defects act as the charge recombination centers and reduce the numbers of effective charges as well as photoactivities²⁹. In addition, thicknesses of the sol-gel-derived TiO_2 films were much thinner than those of P-25 TiO_2 films and wall thicknesses of porous TiO_2 . The high transparency of the thin films also enhances the utilization of activation light and improves photoactivities of the sol-gel-derived TiO_2 films³⁰.

The specific photocatalytic activities of bone-skin-like $\text{SiO}_2/\text{P-25}$ were slightly lower than that of bone-skin-like $\text{SiO}_2/\text{TiO}_2$. The three-dimensional porous architectures with interconnected channels can apply efficient transport paths for pollutant molecules to photocatalytic active sites on the TiO_2 walls^{23,31}. Although the porous $\text{SiO}_2/\text{P-25}$ photocatalysts had similar specific photoactivities with porous $\text{SiO}_2/\text{TiO}_2$ photocatalysts. The blocking of pores leading to the decrease of surface area and pore volume of porous $\text{SiO}_2/\text{P-25}$ materials would lose the above advantage of three-dimensional porous architectures. The large TiO_2 particles formed the non-uniform and rough surface coating onto porous SiO_2 may easily desorb and be attrited during long usage. Those phenomenons may limit the further applications of porous $\text{SiO}_2/\text{P-25}$ materials.

Table 4-7 The weight percentages of silica and titania and the real contents of TiO₂ in bone-skin-like porous photocatalysts with different precursor concentrations.

Samples (TTIP/ isopropanol weight ratio)	Elements		Mass of TiO₂^b (mg)
	Si (%)	Ti (%)	
Porous SiO ₂ /TiO ₂ (0.2)	25.2	4.6	2.3
Porous SiO ₂ /TiO ₂ (0.6)	25.0	8.0	3.6
Porous SiO ₂ /TiO ₂ (1.2)	26.7	11.3	4.5
Porous SiO ₂ /P-25 (0.2)	19.5	20.0	7.6
Porous SiO ₂ /P-25 (0.6)	14.8	26.3	9.6
Porous SiO ₂ /P-25 (1.2)	10.5	34.0	11.5

^b The real mass of titania contained in 15 mg of bone-skin-like photocatalysts.

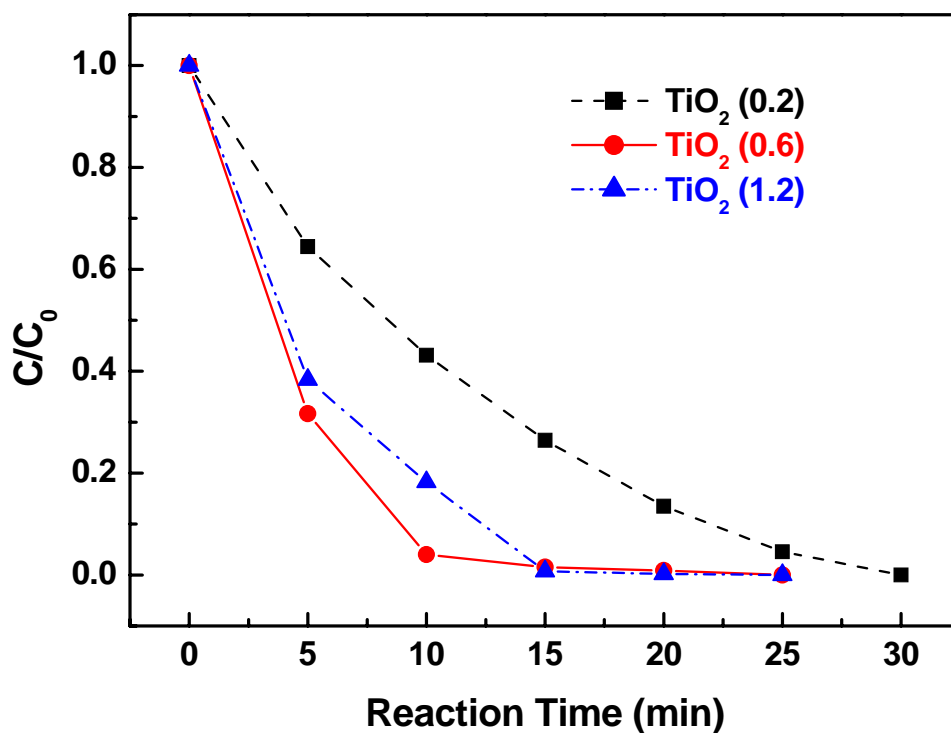


Figure 4-18 The photocatalytic activities of porous TiO₂ with various weight ratios of alkoxide/ solvent.

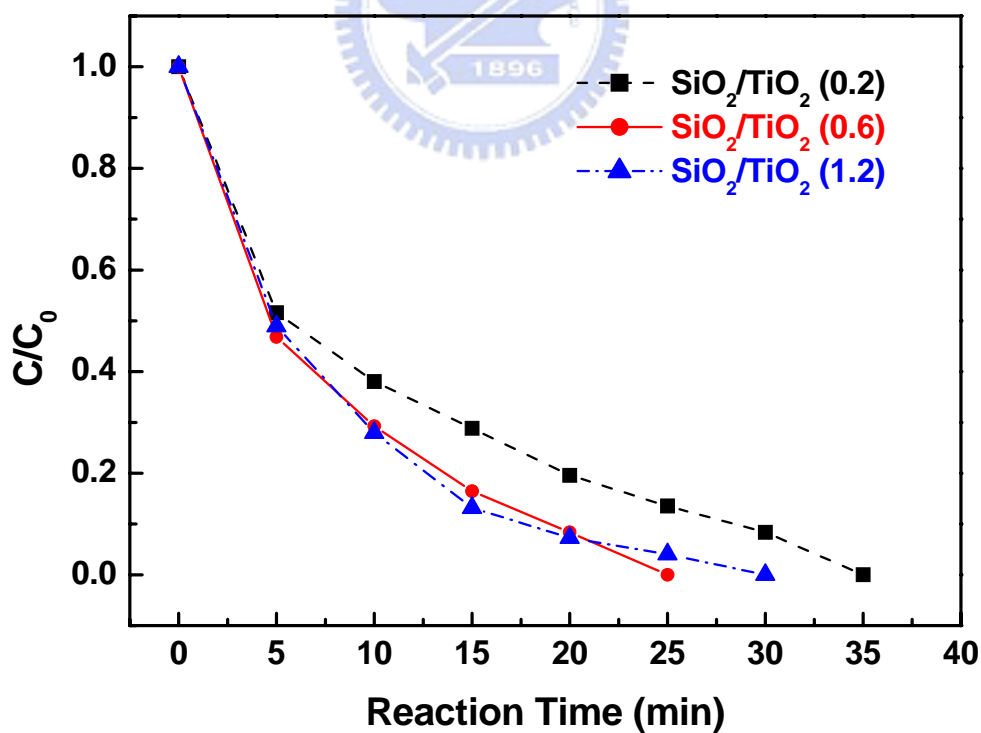


Figure 4-19 The photocatalytic activities of porous SiO₂/TiO₂ with various weight ratios of alkoxide/ solvent.

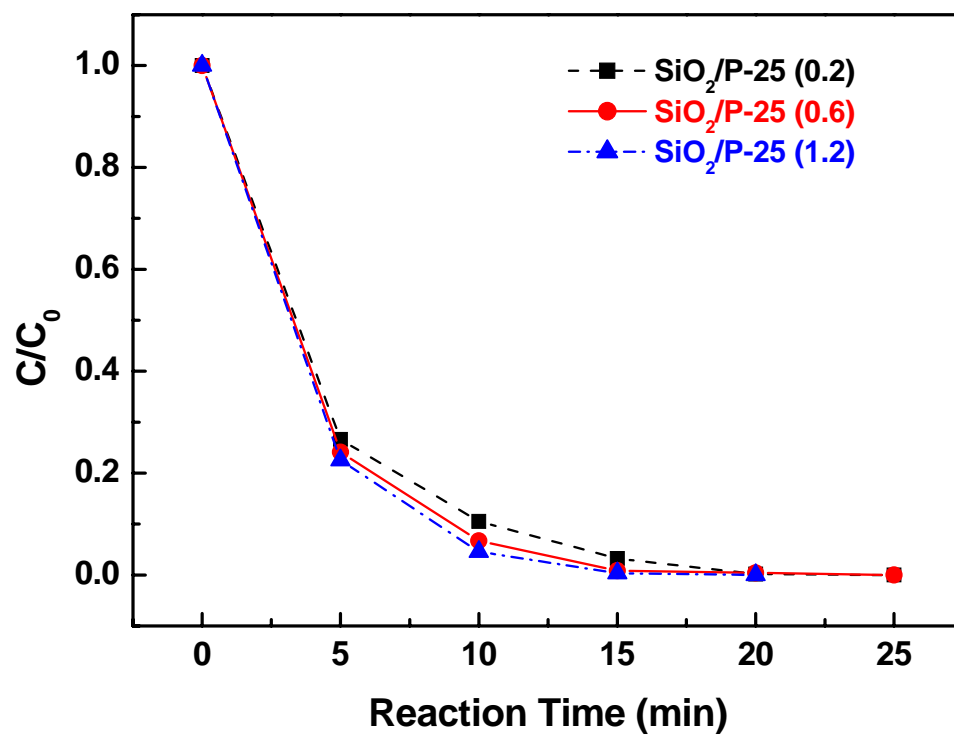


Figure 4-20 The photocatalytic activities of porous SiO₂/P-25 with various weight ratios of alkoxide/ solvent.



Table 4-8 The photocatalytic activities of various porous photocatalysts.

Sample (TTIP/ isopropanol weight ratio)	Degradation rate constant (min⁻¹)	Specific Photoactivities^c (min⁻¹mg⁻¹)
Porous TiO ₂ (0.2)	1.1×10 ⁻¹	7.3×10 ⁻³
Porous TiO ₂ (0.6)	3.0×10 ⁻¹	2.0×10 ⁻²
Porous TiO ₂ (1.2)	2.7×10 ⁻¹	1.8×10 ⁻²
Porous SiO ₂ /TiO ₂ (0.2)	8.3×10 ⁻²	3.6×10 ⁻²
Porous SiO ₂ /TiO ₂ (0.6)	1.2×10 ⁻¹	3.3×10 ⁻²
Porous SiO ₂ /TiO ₂ (1.2)	1.3×10 ⁻¹	2.9×10 ⁻²
Porous SiO ₂ /P-25 (0.2)	2.6×10 ⁻¹	3.4×10 ⁻²
Porous SiO ₂ /P-25 (0.6)	2.9×10 ⁻¹	3.0×10 ⁻²
Porous SiO ₂ /P-25 (1.2)	3.1×10 ⁻¹	2.7×10 ⁻²

^cThe specific photoactivities obtained by normalizing the real mass of titania contained in 15 mg of all porous photocatalysts

Chapter 5. Conclusions

In this study, the high photoactive TiO₂ catalysts with bone-skin-like structure have been successfully prepared using templating sol-gel combined with surface sol-gel method. The thickness of sol-gel-derived TiO₂ film can be well-controlled by varying the concentrations of the TiO₂ precursors in the surface sol-gel process.

The bone-skin-like porous SiO₂/TiO₂ with larger surface area can offer more active sites to adsorb water and hydroxyl groups and result in the higher photocatalytic activities. The sol-gel-derived TiO₂ thin films with high transparency enhance the utilization of activation light and improve the photoefficiencies. Low amounts of bulk defects of the sol-gel-derived TiO₂ films corresponded to the less charge recombination centers and maintained the numbers of effective charges as well as photoactivities. The bone-skin-like porous SiO₂/TiO₂ with ordered hexagonal porous structures in three dimensions can facilitate the transportation of pollutant molecules to photocatalytic active sites on the TiO₂ walls. Moreover, the higher specific weight of composite SiO₂/TiO₂ than that of pure TiO₂ can facilitate the filtration for recovering the catalysts.

The bone-skin-like SiO₂/TiO₂ can not only retain the advantages of porous materials resulting in high specific photocatalytic activities but also overcome the limitations of traditional photocatalysts. These beneficial properties of bone-skin-like SiO₂/TiO₂ can facilitate its applications in the further.

Literature Cited

- (1) Coronado, J. M.; Maira, A. J.; Conesa, J. C.; Yeung, K. L.; Augugliaro, V.; Soria, J. *Langmuir* **2001**, *17*, 5368.
- (2) Li, G.; Zhao, X. S. *Industrial & Engineering Chemistry Research* **2006**, *45*, 3569.
- (3) Bideau, M.; Claudel, B.; Dubien, C.; Faure, L.; Kazouan, H. *Journal of Photochemistry and Photobiology a-Chemistry* **1995**, *91*, 137.
- (4) Dijkstra, M. F. J.; Buwalda, H.; de Jong, A. W. F.; Michorius, A.; Winkelman, J. G. M.; Beenackers, A. A. C. M. *Chemical Engineering Science* **2001**, *56*, 547.
- (5) Balasubramanian, G.; Dionysiou, D. D.; Suidan, M. T.; Baudin, I.; Audin, B.; Laine, J. M. *Applied Catalysis B-Environmental* **2004**, *47*, 73.
- (6) Yu, J. C.; Wang, X. C.; Fu, X. Z. *Chemistry of Materials* **2004**, *16*, 1523.
- (7) Kabra, K.; Chaudhary, R.; Sawhney, R. L. *Industrial & Engineering Chemistry Research* **2004**, *43*, 7683.
- (8) Gonzalez, M. A.; Howell, S. G.; Sikdar, S. K. *Journal of Catalysis* **1999**, *183*, 159.
- (9) Litter, M. I. *Applied Catalysis B-Environmental* **1999**, *23*, 89.
- (10) Linsebigler, A. L.; Lu, G. Q.; Yates, J. T. *Chemical Reviews* **1995**, *95*, 735.
- (11) Yi, G. R.; Moon, J. H.; Yang, S. M. *Chemistry of Materials* **2001**, *13*, 2613.
- (12) Hoa, M. L. K.; Lu, M. H.; Zhang, Y. *Advances in Colloid and Interface Science* **2006**, *121*, 9.
- (13) Velev, O. D.; Lenhoff, A. M. *Current Opinion in Colloid & Interface Science* **2000**, *5*, 56.
- (14) Kuai, S. L.; Bader, G.; Hache, A.; Truong, V. V.; Hu, X. F. *Thin Solid Films* **2005**, *483*, 136.
- (15) Bardosova, M.; Tredgold, R. H. *Journal of Materials Chemistry* **2002**, *12*, 2835.
- (16) Lu, Z. L.; Lindner, E.; Mayer, H. A. *Chemical Reviews* **2002**, *102*, 3543.
- (17) Silva, C. R.; Airoidi, C. *Journal of Colloid and Interface Science* **1997**, *195*, 381.
- (18) Asomoza, M.; Dominguez, M. P.; Solis, S.; Lara, V. H.; Bosch, P.; Lopez, T. *Materials Letters* **1998**, *36*, 249.
- (19) Ichinose, I.; Senzu, H.; Kunitake, T. *Chemistry of Materials* **1997**, *9*, 1296.
- (20) Carbajo, M. C.; Gomez, A.; Torralvo, M. J.; Enciso, E. *Journal of Materials Chemistry* **2002**, *12*, 2740.
- (21) Carbajo, M. C.; Lopez, C.; Gomez, A.; Enciso, E.; Torralvo, M. J. *Journal of Materials Chemistry* **2003**, *13*, 2311.
- (22) Asilturk, M.; Sayilkan, F.; Erdemoglu, S.; Akarsu, M.; Sayilkan, H.; Erdemoglu, M.; Arpac, E. *Journal of Hazardous Materials* **2006**, *129*, 164.
- (23) Holland, B. T.; Blanford, C. F.; Do, T.; Stein, A. *Chemistry of Materials* **1999**, *11*, 795.

(24) Lee, B.; Lu, D. L.; Kondo, J. N.; Domen, K. *Journal of the American Chemical Society* **2002**, *124*, 11256.

(25) Hoffmann, M. R.; Martin, S. T.; Choi, W. Y.; Bahnemann, D. W. *Chemical Reviews* **1995**, *95*, 69.

(26) Gesenhues, U. *Journal of Physics and Chemistry of Solids* **2007**, *68*, 224.

(27) Tada, H.; Tanaka, M. *Langmuir* **1997**, *13*, 360.

(28) Nakade, S.; Saito, Y.; Kubo, W.; Kitamura, T.; Wada, Y.; Yanagida, S. *Journal of Physical Chemistry B* **2003**, *107*, 8607.

(29) Adachi, M.; Murata, Y.; Takao, J.; Jiu, J. T.; Sakamoto, M.; Wang, F. M. *Journal of the American Chemical Society* **2004**, *126*, 14943.

(30) Cen, H. W.; Li, X. J.; He, M. X.; Zheng, S. J.; Feng, M. Z. *Chemosphere* **2006**, *62*, 810.

(31) Stathatos, E.; Petrova, T.; Lianos, P. *Langmuir* **2001**, *17*, 5025.



Appendix A. Operational parameters of the instruments



Appendix A-1. The operational parameters of XRD

Parameters	Values
Scan range (degree)	20~90 degree (2~120)
Sampling Width (degree)	0.02
San Speed (degree/min)	4.0
Measurement type	Ordinary (without background)
Theta angle Set	OFF
Voltage (kV)	30
Current (mA)	20
Divergence slit	1.0 degree
Scatter slit	1.0 degree
Reveiving slit	0.3 mm

Scherrer's equation

$$D = \frac{0.89 \times 0.15406}{\beta \times \cos \theta}$$

D: diameter of crystals

X-ray source: wavelength of Cu $k\alpha = 0.15406$ nm

β : FWHM (calculated from XPSPEAK41) $\times (\pi/180)$

Appendix A-2. The operational parameters of UV-Vis.

Parameters	Values
Measurement	Wavelength scan
Data Mode	%R
Starting Wavelength	800 nm
Ending Wavelength	200 nm
Scan speed	300 nm/min
Sampling Interval	1 nm
Slit Width	1 nm
PMT Voltage	Auto
Lamp Change	340 nm
Base line correction	User 1
High Resolution	On
Reference	Al ₂ O ₃

Kubelka-Munk formula¹⁷

$$F(R) = \frac{(1 - R)^2}{2R} = \frac{k}{S}$$

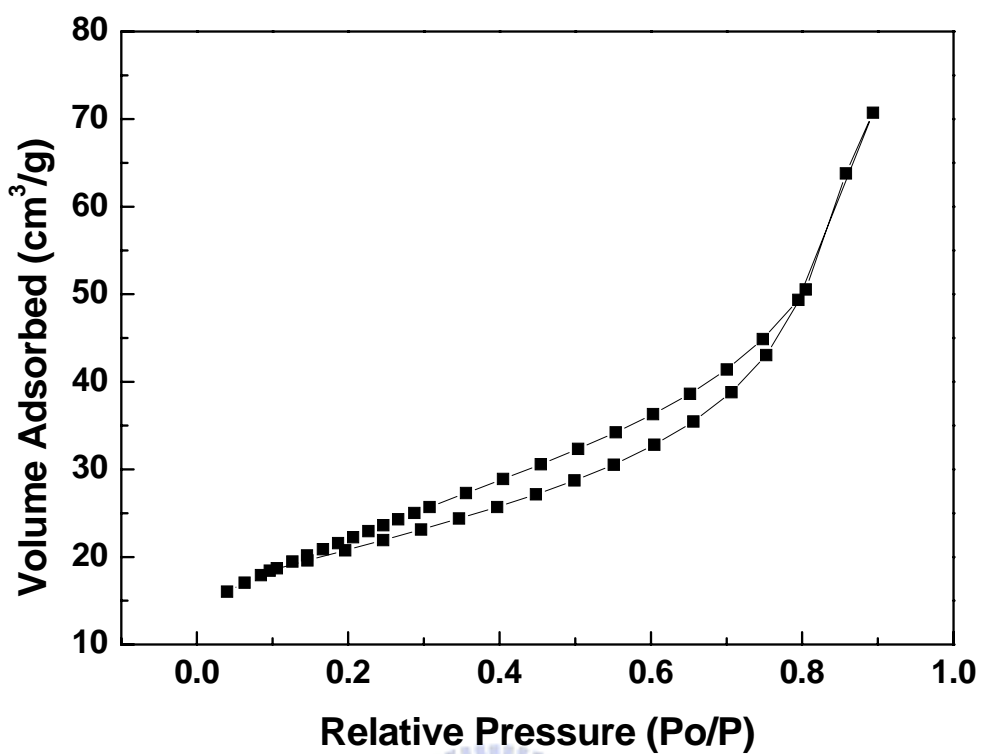
k: absorption coefficient

S: scattering coefficient

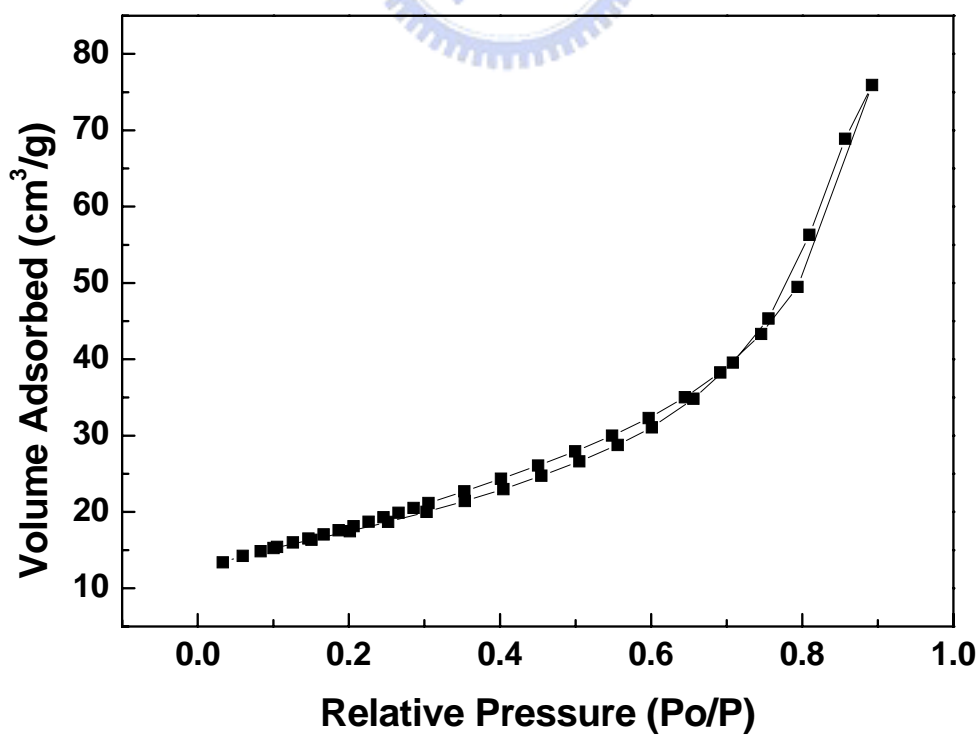
R: %R reflectance

Appendix B. Nitrogen adsorption-desorption isotherms



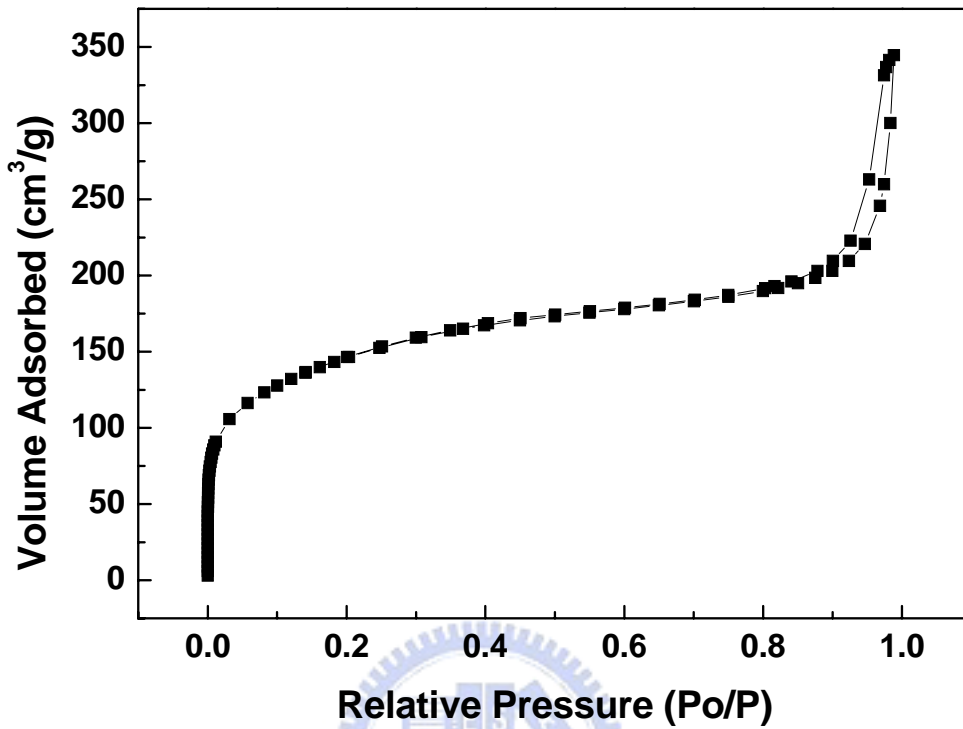


Appendix B-1. The nitrogen adsorption-desorption isotherm of porous TiO₂ with the precursor concentration of 0.2.

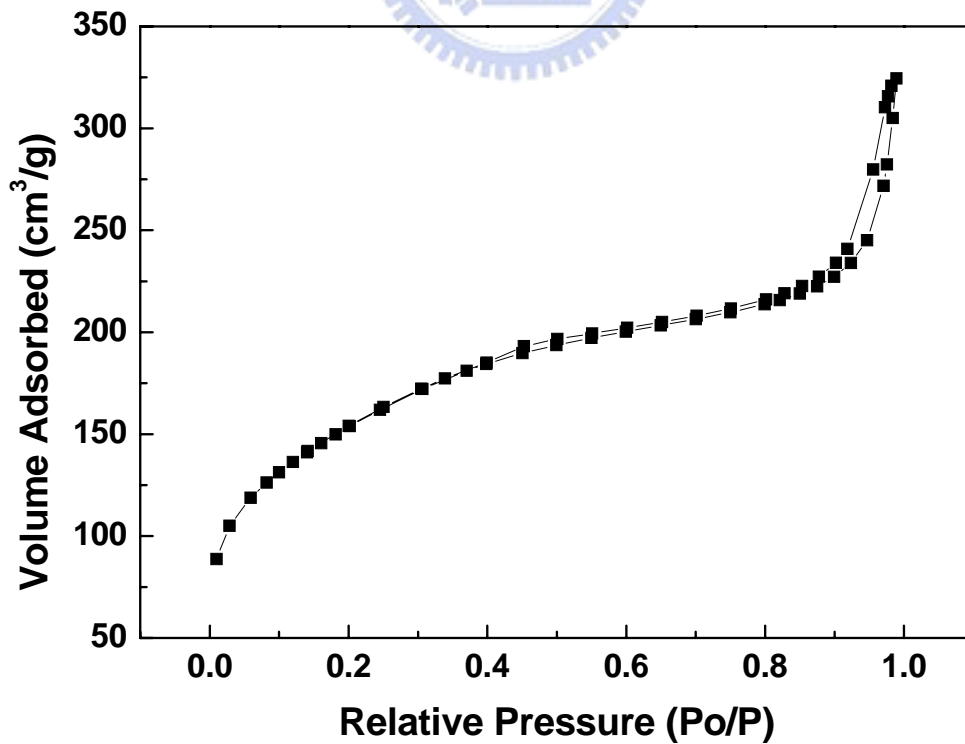


Appendix B-2. The nitrogen adsorption-desorption isotherm of porous TiO₂ with the

precursor concentration of 1.2.

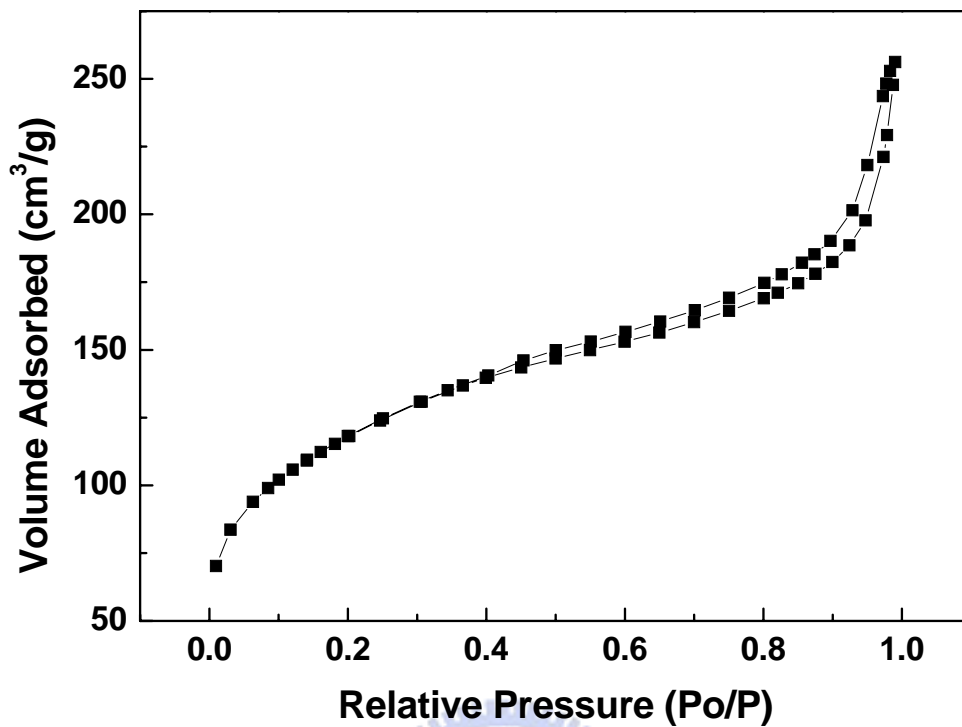


Appendix B-3. The nitrogen adsorption-desorption isotherm of porous SiO₂.

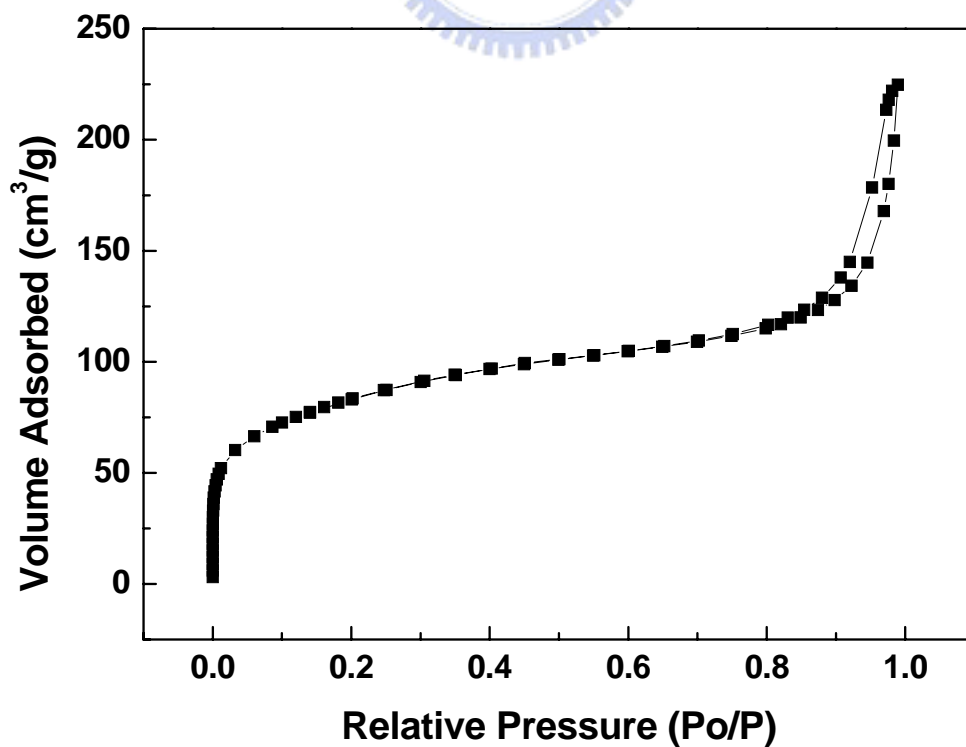


Appendix B-4. The nitrogen adsorption-desorption isotherm of porous SiO₂/TiO₂ with the

precursor concentration of 0.2

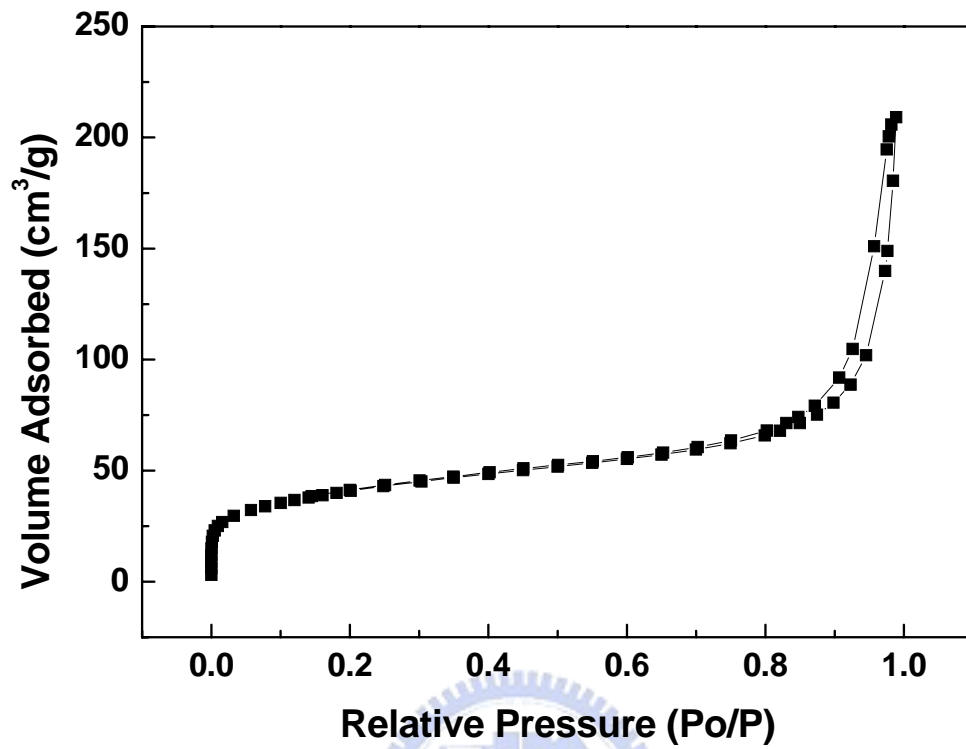


Appendix B-5. The nitrogen adsorption-desorption isotherm of porous SiO₂/TiO₂ with the precursor concentration of 1.2



Appendix B-6. shows the nitrogen adsorption-desorption isotherm of porous SiO₂/P-25

with the TiO₂ concentration of 0.2.



Appendix B-7. shows the nitrogen adsorption-desorption isotherm of porous SiO₂/P-25 with the TiO₂ concentration of 1.2.

